Theses and Dissertations

8-2013

Insights into the Timing, Origin, and Deformation of the Highland Mountains Gneiss Dome in Southwestern Montana, USA

Lane Markes Boyer
University of Arkansas, Fayetteville

Insights into the Timing, Origin, and Deformation of the Highland Mountains Gneiss Dome in Southwestern Montana, USA

Insights into the Timing, Origin, and Deformation of the Highland Mountains Gneiss Dome in Southwestern Montana, USA

A thesis submitted in partial fulfillment
of the requirements for the degree of
Master of Science in Geology

By

Lane Markes Boyer
University of Arkansas
Bachelor of Science in Geology, 2011

August 2013
University of Arkansas

This thesis is approved for recommendation to the Graduate Council.

_____
Dr. Gregory Dumond
Thesis Director

_____
Dr. Margaret Guccione
Committee Member

_____
Dr. Steve Boss
Committee Member

Abstract

The Highland Mountains of southwestern Montana offer a unique view of the Archean igneous and metamorphic rocks within the Great Falls tectonic zone (GFTZ). A Paleoproterozoic structural gneiss dome has been interpreted in the southern extent of the Highland Mountains. The ~ 130km^2 of exhumed metamorphic rocks and gneiss dome exposed in the Highland Mountains are the primary focus of this research. The formation of the Highland Mountains gneiss dome is proposed to be directly related to a northwest-side down detachment (the Steels Pass shear zone) that formed during terrane collision along the GFTZ. The field investigation determined foliation and lineation orientation measurements taken at 65 stations. Twenty-two field oriented samples were obtained from a variety of rock types distributed across the ~ 24 km^2 field area. Three field-based domains were established from the lithology, foliation, and lineation observations. Full-section X-ray maps of three sample thin-sections were collected via EPMA to identify all monazite grains. Twenty-eight grains were mapped at high-spatial resolution (0.3–6.0 μm). Thin section micro-structures observed show effects of a multistage deformation history with both dynamic and static recrystallization processes. Monazite geochronology of one thin section revealed two distinct populations of monazite grains; Archean (~ 2.5 Ga) and Mesoproterozoic (~ 1.5 Ga). The older population represents the crystallization age of either, or both the Medicine Hat block and the Wyoming province terranes. The younger population is hypothesized to have grown during deformation/alteration associated with the formation of the Belt-Purcell Rift Basin.

Acknowledgements

I would like to thank my friend and advisor Greg for his time and guidance, Peggy for the use of her wonderful Montana ranch, and Steve for his support and comments. This project would never have left the office without you.

I would also like to thank my friends and family for sticking with me through this project.

Table of Contents

I. Introduction

Gneiss dome development during (and after) orogeny remains a significant field of study in tectonics, e.g., the Himalayas (e.g. Beaumont et al., 2004). Gneiss domes have been inferred to occur during both continental collision and extension (Beaumont et al., 2001; Andronicos et al., 2003). Critical to understanding the tectonic significance of gneiss domes, is the study of well-exposed samples from the geologic record that can be linked to plate collision and/or extension.

A Paleoproterozoic structural gneiss dome has been interpreted in the southern extent of the Highland Mountains, Montana, within the Great Falls tectonic zone (GFTZ) (O'Neill et al., 1988; O'Neill et al., 1996; Figures 1A and 1B). The GFTZ is a northeast-trending zone of geologic features that can be traced from the Idaho Batholith, across the Laramide thrust-belt and basement structures of southwestern Montana, through the cratonic rocks of central Montana and into southwestern Saskatchewan, Canada (O'Neill, 1985; Figure 2). The GFTZ and the Vulcan structure ~ 800 km to the north, have both been proposed as sites of a Paleoproterozoic suture between the Archean Hearne and Wyoming provinces (Mueller et al. 2005; Figure 3). Virtually all of the Precambrian rocks composing the Vulcan structure and much of the GFTZ are buried beneath Phanerozoic cover. The primary exceptions to this are igneous and metamorphic rocks of the Highland Mountains and the Little Belt Mountains of Montana (Mueller, 2002). Thus the ~ 130 km^2 of exhumed metamorphic rocks and gneiss dome exposed in the Highland Mountains are a window into the structures of the GFTZ and are the primary focus of this research (Figures 1A and 1B).

The main objective of this project was to define the tectonic relationship between the Highland Mountains gneiss dome and the formation of the GFTZ of southwest Montana. The

1

formation of the Highland Mountains gneiss dome is hypothesized to be directly related to a northwest-side down detachment (shear zone) that formed during terrane collision along the GFTZ. Unfortunately, the exact boundaries and the timing and nature of dome formation are not well understood. The primary purpose of this project was to determine if the Highland Mountains gneiss dome formed within the tectonic context of the Paleoproterozoic collision between the Wyoming and Hearne/Medicine Hat provinces along the GFTZ. (e.g. O'Neill et al., 1988; O'Neill, 1995; Foster et al., 2006; Harms et al. 2006)

II. Geologic Setting

The Precambrian geology of North America is characterized by geochemically and geophysically distinct Archean cratonic blocks bounded by Proterozoic orogenic zones (and inferred suture zones) resulting from collisions with Paleoproterozoic terranes or other Archean cratons (Karlstrom and Houston, 1984; Chamberlain, 1998; Nelson et al., 1993; Dahl et al., 1999). The primary geologic components of the upper midwestern United States and southwestern Canada include the Superior province, the Hearne province, Wyoming province, and the Medicine Hat block terranes, as well as the Great Falls tectonic zone, the Trans-Hudson orogen, and the Vulcan structure orogenic zones (Figure 3; Mueller, 2002; Foster et al., 2006). The interaction between these blocks and provinces during collision of the Wyoming and Hearne provinces is not well constrained (Mueller, 2002). Several models have been proposed to explain the suturing/interaction of these provinces. Mueller (2002) suggested an "en-echelon" amalgamation of the Wyoming, Medicine Hat, and Hearne provinces. He suggested that the collision between the Wyoming craton and Medicine Hat terrane occurred first in the Archean along the GFTZ, followed by suturing of the Wyoming-Medicine Hat composite block with the

Hearne province (Green et al., 1985; Hoffman, 1988; Boerner et al., 1998; Lemieux et al., 2000). An alternative model proposed by O'Neill and Lopez (1985) and O'Neill (1988) suggested that the Medicine Hat block docked first with the Hearne province along the Vulcan structure, followed by a later (pre-Mesoproterzoic) collision of the Medicine Hat/Hearne composite block with the Wyoming province along the GFTZ.

The Highland Mountains, situated within the GFTZ, include some of the westernmost exposures of metamorphic Archean basement in southwestern Montana and thus possible exposures of the orogen between the Wyoming and Medicine Hat/Hearne provinces (Harlan et al., 1996). The rocks consist of a layered sequence of amphibolite-grade leucocratic gneiss, overlain by well-foliated quartz+feldspar+biotite gneiss (Harlan et al., 1996). In general, the layered metamorphic rocks of the southern Highland Mountains define a large doubly-plunging antiform (O'Neill et al., 1988). The antiform structure, called the Highland Mountains gneiss dome by O'Neill et al. (1988), was interpreted to have formed as a result of a poorly understood regional metamorphic event during penetrative deformation at ca. 1.8 Ga, which reset the K-Ar and Rb-Sr mineral systems in Archean basement rocks across much of southwestern Montana (Gilletti, 1966, 1971; Erslev and Sutter, 1990). This was coincident with the Big Sky orogeny, as defined in the Tobacco Root Mountains to the northeast of the study area (Harms et al, 2004).

The rocks of primary importance to this study include leucogranite sills and dikes comprising the "sill complex" unit within the gneiss dome of the southern Highland Mountains as mapped by O'Neill et al. (1996) in the vicinity of Steels Pass (rectangle in Figure 1B). O'Neill et al. (1996) describe this unit as a "dense swarm of leucocratic quartz-feldspar sills intruded into crystalline metamorphic rocks. The sills are present both as non-foliated, coarse-grained pegmatite and as strongly sheared, lineated, and foliated mylonitic intrusions." The

metamorphic rocks of this sill complex unit are proposed to coincide with a detachment/shear zone that accommodated exhumation and formation of the Highland Mountains gneiss dome (O'Neill et al., 1988). This detachment will be referred to as the Steels Pass shear zone.

III. Background

The age and origin of the Highland Mountains is only loosely constrained in the literature. Harlan et al. (1996) found that $^{40}Ar/^{39}Ar$ dates for biotite and hornblende in basement gneiss from the southern Highland Mountains record cooling ages of 1820 – 1793 Ma. This date was proposed to be the record of cooling of the Highland Mountains gneiss dome following high-grade metamorphism in early Proterozoic time (Harlan et al., 1996). U-Pb geochronological constraints from the Highland Mountains are extremely limited. U-Pb dates from zircons sampled in gneisses of the southern Highland Mountains record two poorly constrained age populations, the first at 2.7 – 3.0 Ga and the second at 1.8 – 1.9 Ga (O'Neill et al., 1988). The latest event was interpreted as the record of metamorphism and deformation of the Highland Mountains gneiss dome during the formation of the GFTZ (O'Neill and Lopez, 1985). The only other published U-Pb data from the Highland Mountains consists of a ca. 1.77 Ga date for monazite from a cross-cutting leucogranite in the quartzofeldspathic host gneiss (Mueller et al., 2005). The limited geochronological data are consistent with Paleoproterozoic tectonism affecting the Highland Mountain gneisses, but the accurate timing of gneiss dome formation and deformation along the GFTZ remain poorly understood.

IV. Methodology

This research addresses two major problems: 1) the relationship between the Highland Mountains gneiss dome and the GFTZ, and 2) the timing of leucogranite emplacement and deformation/alteration within the Highland Mountains gneiss dome. Data were compiled from previous studies and a foliation trajectory map was constructed to help constrain the relationship between the Highlands gneiss dome and the northeast-trending GFTZ (Figure 1B). Regional geologic mapping and structure contouring outline the extent and orientation of the Highland Mountains gneiss dome. Stereonet analyses and cross-sections constrain the geometry of the dome in the focus area (rectangle in Figure 1B). Mapping and in-situ analysis of syn-kinematic (grown during deformation) monazite in field-oriented tectonites (metamorphic rocks highly altered due to tectonic activity) constrains the timing and nature of the hypothesized Paleoproterozoic deformation.

Field Methods

The month-long field investigation focused on the NW-dipping Steels Pass shear zone first noted by O'Neill et al. (1988). Observations included the orientation of gneissic fabrics, mineral lineations, and a detailed field survey of the Paleoproterozoic leucogranite sill complex. The field area was located at ~ 2500 m elevation with the vast majority of the area thickly vegetated with high-altitude grasses greatly limiting the outcrop exposure. Foliation and lineation orientation measurements were taken at 65 stations distributed across the ~ 24 km^2 field area (Figure 4). Measurements from the field investigation and also those data recorded by O'Neill et al. (1985) were contoured to provide an interpretive structure / foliation trajectory map (Figure 5). Field measurements were incorporated into the conceptual cross section A-A' and

plotted/analyzed using the OSX Stereonet 8.0.2 © 2011-2012 software package created by R. W. Allmendinger (Figure 6). Twenty-two field-oriented samples were taken from a variety of rock types distributed across the field area. The data provided structural constraints on the relationship between the deformation of the Highlands gneiss dome and the emplacement of the leucogranite sill complex in the context of the GFTZ. To understand the timing of leucogranite emplacement and deformation of the Highlands gneiss dome, we collected field-oriented samples from (1) the leucogranite sill complex, (2) the deformed gneisses hosting the sill complex, and (3) a garnet-rich leucocratic gneiss approximately 5 km south of the map area. Slabs of the samples were cut perpendicular to foliation and parallel to the stretching lineation to identify sense of shear and the textural setting of monazite (e.g. Passchier and Trouw, 2005). For ten select samples, polished thin sections were professionally prepared by Burnham Petrographics for optical petrography and in-situ electron probe microanalysis (EPMA). Backscattered electron (BSE) imaging, X-ray mapping, and quantitative analyses of monazite were done using the Cameca® SX50 and Cameca® "Ultrachron" electron microprobe at the University of Massachusetts Electron Microprobe Lab, Amherst, Massachusetts. Emphasis was placed on identifying oscillatory- or sector-zoned monazite in the leucogranites to date the time of crystallization, and defining domains of monazite in host gneisses that grew syn-kinematically with deformation and metamorphism (e.g., Dumond et al. 2008).

Monazite Geochronology Methods

Monazite Th–U–total Pb geochronology by EPMA in this study followed the strategy proposed by Williams et al. (2006). Monazite geochronology works on the basis of two fundamental assumptions 1) All Pb measured in the sample is radiogenic, having formed from

the decay of its parent elements U or Th. 2) Monazite behaved as a closed system since the time

of crystallization.   Concentrations (ppm) of U, Th, and Pb are measured via the electron

microprobe, these values are then plugged into the age equation (*Equation 1*) to produce a date

(τ). λ^{232}, λ^{238}, and λ^{235} are the decay constants of ^{232}Th, ^{238}U, and ^{235}U respectively (Montel et al.,

1996).

Equation 1

$$Pb = \frac{Th}{232}[\exp(\lambda^{232}\tau) - 1]208 + \frac{U}{238.04}0.9928[\exp(\lambda^{238}\tau) - 1]206 + \frac{U}{238.04}0.0072[\exp(\lambda^{235}\tau) - 1]207$$

Full-section Ca Kα maps of thin-sections 12B-46B, 12B-15B and MT11-01 were

collected via EPMA to identify all monazite grains (Figures 7, 8, and 9; Williams and Jercinovic,

2002). Twenty-eight grains were mapped at high-spatial resolution (0.3–6.0 µm) (Figures 7, 8,

and 9). Y Lα and Th Mα maps were batch-processed simultaneously and individually to identify

similar and texturally distinct compositional domains to guide subsequent quantitative analysis

(Williams et al., 2006). All quantitative trace element analyses were preceded by high-resolution

wavelength spectral scans and peak overlap corrections following the methods of Jercinovic and

Williams (2005) and Jercinovic et al. (2008) (see also Pyle et al., 2005). All background scans

and quantitative analyses were carried out with a focused beam at 15 kV and 200 nA using a

modified Cameca® SX100 electron microprobe - the Cameca® "Ultrachron" EPMA. For details

regarding the instrument, analytical protocol, and standards used, see Jercinovic et al., 2008. A

2σ standard deviation uncertainty for each dated domian is reported (Figure 10).   The final result

is illustrated as a single histogram probability distribution for each monazite domain. Multiple

domains from one or more grains (interpreted to represent the same monazite growth event based

on similarity in date, composition, and/or texture) were grouped together based on a bin size of 100 million years (Figure 11). Multiple results from a consistency standard of known age are presented along with the data to document short-term systematic error and provide a qualitative assessment of accuracy during the analytical session (Williams et al., 2006).

V. Results

Field Data

Field mapping of the Steels Pass area revealed a suite of geologic features affected by multiple deformation events that have occurred since the Neoarchean. Foliation and lineation measurements were divided into three field-based domains based on the mapped lithology and structural setting.

Domain 1

Domain 1 included the Early Proterozoic and Archean mylonitic biotite gneiss (X(A)m) and a thin (0.5km-wide) swath of the Early Proterozoic and Archean quartz + feldspar + biotite gneiss (X(A)qf) exposed north of the Early Proterozoic sill complex (Xs(X(A)qf)) (Figures 4-6). This domain is defined by the relative absence of clear stretching lineations and or leucogranite sills. Measurements were restricted by access and outcrop exposure to the ridgeline of the ~ 700 m high Big Ridge trending NW-SE for ~ 5 km through the central map area. Fabric seen in domain 1 is defined by the prevalent fine sheets of biotite and the occasional quartz ribbon and/or plagioclase clast (Figure 12). This domain contains 20 data locations which reveal a mean foliation orientation of 198°, 26°W and a mean lineation orientation of 15° → 199° (Figure 6). In this domain a measureable stretching lineation was only found in three site locations due to the biotite-rich schistose nature of the gneisses. Domain 1 contained very few site locations in

which clear kinematic observations could be made, but where clast kinematics could be

measured a top-down-to-the-west sense of motion was indicated (Figure 13).

Domain 2

Domain 2 is defined by the persistence of a clear, down-plunge stretching lineation

observed in many of the 24 data locations mapped within the sill complex unit (Figures 4-6).

This area consists of Early Proterozoic quartz + feldspar + biotite gneiss that has been

pervasively intruded by leucogranite and mafic sills (Figures 14 and 15). Measurements in this

domain were predominantly taken in the area immediately north of Steels Pass and further

northeast on Brazil Ridge. Observations made in both areas confirm the NNE extent of the

Steels Pass shear zone. Domain 2 has a mean foliation of 209°, 22°W and a mean lineation of

22° → 261° (Figure 6). The fabric of domain 2 is defined by stringers of biotite, quartz ribbons

and flattened/stretched clasts of plagioclase feldspar (Figure 16). Within Domain 2, the

measurable lineations are distinctly defined by a tightly clustered, direct down-plunge, western

orientation on the stereonet (Figure 6). Lineations are primarily visible in the leucogranite sills

that intruded the host gneiss (Figure 17). These lineations were closely analyzed and were

interpreted to be dominantly a line of stretch due to tapered feldspar clasts and elongate ribbons

of quartz. In this area the leucogranite sills include abundant deformed plagioclase clasts, which

also uniformly indicate a top-down-to-the-west sense of shear (Figures 16 and 18).

Domain 3

Domain 3 includes all 31 data points south of the sill complex unit in the quartz +

feldspar + biotite gneiss (Figures 4-6). The western extent of domain 3 is delineated by the west-

dipping limb of an antiform structure. This area is intruded by both leucogranite and mafic sills,

which occur at approximately the same frequency, as opposed to the previous two domains in

which exposures of the leucogranite sills appear to greatly outnumber the mafic sills. Also included within this domain is an Early Proterozoic mafic body (Xm). Field measurements identify a sub-horizontal, upright, antiformal structure with a best-fit girdle calculated to be 339°, 87°E and with a SW-plunging β-axis of 03° → 249° (Figure 6). Parasitic folds are prevalent on both the east and west limbs of the antiform (Figure 19). The antiform structure is truncated in the north and south by the Hell Canyon Pluton (TKqmh) and the Twin Bridges Fault, respectively. A clear overprinting of an older vertical fabric (S_1~ 064˚, 90˚) by a younger, much shallower fabric (S_2 ~ 180˚, 3˚W) is evident across this domain (Figure 20). Identifiable clast kinematics are rarely observed, although a stretching or intersection lineation is consistently definable that plunges both east and west in the respective limbs of the antiform.

Thin Section Data

Domain 1

One thin section was cut from a garnet + biotite gneiss (sample 12B-15B) collected in domain 1 (Figure 21). Major mineral components include: ~ 50% quartz, ~ 25% garnet, ~ 15% biotite, and ~ 10% plagioclase + K-feldspars. The fabric in this thin section is defined by quartz ribbons ~ 1.0 mm in width with biotite plates conforming to the delineated fabric orientation. Garnet is present, but pervasively replaced by biotite.

Domain 2

Six of the ten thin sections prepared were cut from samples sourced from domain 2. Four samples were taken from leucogranite sills and the other two thin sections are from mafic granulite sills. Thin section 12B-01 from a leucogranite sill near Steels Pass exhibits excellent clast kinematics (Figure 22). The fabric in 12B-01 is defined by elongate quartz ribbons. Major

mineral components include: ~ 90% quartz, ~ 5% plagioclase, ~ 5% biotite. Some plagioclase clast cores have been completely replaced by clusters of new small grains. Core-mantle structures apparent in the larger syn-kinematic plagioclase clasts range from 2-5 mm in diameter. In contrast, recrystallized mantle clasts are substantially smaller, ~ 350 – 550 μm in diameter. Matrix grains are ~ 125 μm in diameter.

A second leucogranite sill within domain 2 found on Brazil Ridge was sampled (thin section 12B-11, Figure 23). Major minerals in this sample include: ~ 60% quartz and ~ 40% plagioclase. The fabric in this section is defined by elongate quartz ribbons and a few large (2.0 – 3.0 mm) quartz clasts. Quartz ribbons and clasts exhibit pervasive undulose extinction. The quartz ribbons vary in size, with the largest ribbons exceeding 20 mm in length and ~ 1.5 mm wide. Plagioclase clasts show core-mantle structures, separating new small mis-aligned plagioclase grains. Core clasts range in size from ~ 3.0 – 4.0 mm in diameter, but recrystallized mantle grains are only 350 – 450 μm. The core and mantle grains are surrounded by a matrix of much finer quartz and plagioclase grains (75 – 100 μm).   Subtle bands of fine-grained matrix are aligned with the fabric extending across the section.

Thin section 12B-46B is also from yet another leucogranite sill ~ 200 m south of the 12B-01 site in the vicinity of Steels Pass (Figure 24). This thin section is of utmost importance because it contains monazite grains, which have been analyzed further and will be discussed in the monazite geochronology section. The fabric in this sample is defined by quartz ribbons, with the largest ones ~ 1 mm x 15 mm in size, with well-developed undulose extinction. Quartz ribbon grains have been recrystallized into polygonal forms. Syn-kinematic K-feldspar and plagioclase clasts show top-down-to-the-west dextral shear. The largest feldspar grains are ~ 1.5 mm in diameter, many of which show severe deformation as cracks and alteration to sericite.

Evidence for core-mantle structures exists, though in this thin section the core grains have been completely recrystallized into new grains with the mantle (350 – 400 μm). Grain boundaries in this sample are convex in shape, likely due to a static recrystallization process discussed later.

Mafic sills were also sampled and thin section 12B-10B is from a mafic granulite sill on Brazil Ridge (Figure 25). Dominant minerals include: ~ 70% hornblende, ~ 10% quartz, ~ 15% garnet remnants, and ~ 5% plagioclase. Garnet is replaced by hornblende, but remnant garnet grains ~ 2 mm in diameter are present. The matrix fabric in this thin section is defined by the grain-shape preferred orientation of the very fine-grained (~ 125 μm) laths of hornblende.

Domain 3

Two thin sections examined are from this domain. Sample 12B-32 is from a leucogranite sill that crosses the east-dipping limb of the antiform (Figure 26). This sample is very coarse grained and composed of ~ 80% quartz, ~ 10% plagioclase, ~ 5% K-feldspar, and ~ 5% biotite. Large quartz clasts with core/mantle structures dominate this section. Core grains are ~ 12 mm in diameter and the smaller mantle grains are ~ 1.0 – 1.5 mm in diameter and the very small matrix grains range in size from 250 to 500 μm in diameter. Fabric in this section is delineated by numerous elongate quartz ribbons, which are ~ 1mm in width and 5mm in length.

Thin section 12B-40 is from a leucogranite sill on the west-dipping limb of the antiform (Figure 27). Core-mantle structures persist with core clasts of 1.5 to 3.5 mm in diameter and mantle grains of 250 – 450 um in diameter. Fabric in this section is defined by quartz ribbons ~ 700 um wide and up to 10 mm in length and with undulose extinction. Grain boundaries outside the quartz ribbons are curved. Mineralolgy includes: ~ 90% quartz, ~ 5% plagioclase, and ~ 5% biotite. Bands in the thin section are rich with platy biotite grains aligned with the rock fabric. The entire section is divided by a pair of micro-faults oriented perpendicular to the fabric.

An additional thin section is MT11-01, from a garnetiferous migmatitic sill approximately 5 kilometers south of the mapping area (Figure 28). The major mineral components of this rock include: ~ 40% quartz, ~ 30% plagioclase + K-feldspar, ~ 20% garnet, ~ 10% biotite. Feldspars display replacement by sericite/muscovite (white micas). This sample has a coarse-grained (1.0 – 3.0 mm) phaneritic texture. Weak fabric is visible due to the elongate quartz grains, which exhibit undulose extinction (sub-grain boundaries). Grain boundaries tend to be nearly perpendicular to fabric.

Monazite Geochronology

Monazite dating analyses were performed on the thin section of leucogranite sill 12B-46B from domain 2. This sample was chosen for the analysis due to its structurally significant field location and the quality of its monazite grains. Five priority grains were dated using the Cameca® "Ultrachron" EPMA. Grains were given priority based on their zoning and condition. Severely altered grains were excluded from the analyses.

Two distinct populations of monazite domains are exhibited in the five monazite grains analyzed (Table 1A-1D; Figure 11). The older population (P1) includes of 11 dates taken from the cores and various zones within four of the analyzed grains. P1 has an average date of 2444.87 ± 392 Ma (Figure 10). These dates may be indicative of inherited Archean monazite grains from the country rock through which the leucogranite sill intruded. The younger population (P2) consists of 6 dates taken from the rims of grains M1, M5, and M7 and the core of grain M6 (Figures 29 and 30). P2 has an average date of 1534.27 ± 116 Ma (Figure 10). Neither of these populations represents the crystallization age of the leucogranite sill dated by Mueller et al. (2005) as ca. 1770 Ma.

VI. Discussion

Research on the Highland Mountains gneiss dome is of particular importance because of its location in the enigmatic GFTZ. This zone is recognized as the northern boundary of the Wyoming cratonic province (O'Neill and Lopez, 1985). Although there is disagreement concerning both the timing and tectonic setting of the formation of the GFTZ (Mueller et al., 2005), it is inferred as the suture zone between the unexposed Archean Medicine Hat block of the Hearne province and the Wyoming craton (Fig. 1A) (O'Neill and Lopez, 1985). Aspects of the Highland Mountains and other Precambrian basement rock in SW Montana resemble those structures found in the Early Proterozoic suture zones of the Canadian Shield (O'Neill, 1998; Hoffman, 1989), where monazite analyses have previously been utilized successfully to date deformation (e.g., Snowbird Tectonic Zone: Dumond et al., 2008). The Archean leucogneisses coring the Highland Mountains are inferred to have experienced Paleoproterozoic strain during collision along the GFTZ (Mueller et al., 2005).

Previously mapped by O'Neill et al. (1996), a structural gneiss dome has been interpreted as underlying much of the southern extent of the Highland Mountains. Previous research in the region has been inconclusive regarding whether the gneiss dome formed directly in response to collision along the GFTZ or as a result of later extension, e.g., as a metamorphic core complex (Foster et al., 2006). The discovery of the Steels Pass shear zone supports the existence and development of the Highland Mountains gneiss dome during post-orogenic extension as a result of crustal thickening. The Steels Pass shear zone, identified by a shallow west-dipping fabric (Figure 14), was formed as the zone of detachment along which the Highland Mountains gneiss dome was exhumed. The activation of the Steels Pass shear zone and the exhumation of the gneiss dome likely were initiated late in the Paleoproterozoic tectonic event history (~ 1.7 Ga:

14

see monazite data interpretation below). The exhumation of the Highland Mountains gneiss dome resulted in lower amphibolite grade metamorphism and partial melting. Post-orogenic extension is commonly associated with lithospheric delamination and mafic magmatism (Collins, 2002). This process could have produced the mafic sills present in the Highland Mountains as underplating mafic material was emplaced between ~ 1.80 and ~ 1.75 Ga in the Medicine Hat block to the northwest (Davis et al. 1995).

Structural Evolution

Across the map area, the three domains defined above are distinctly visible in the foliation trajectories. Domain 1 includes a penetrative fabric which is consistently oriented at around 198˚, 26˚W (Figure 6). This is interpreted to be the background host gneiss fabric, i.e., pre-emplacement of the leucogranites and a relict feature of the Neoarchean?-Paleoproterozoic metamorphic history of the mylonitic bioite-gniess.

Further south, the transition from domain 1 into domain 2 is marked by the abrupt increase in leucogranite sills and the definition of a well-defined stretching lineation (Figures 4-6). The stretching lineations in domain 2 sills define the NNE trending Steels Pass shear zone as a zone of dextral shear sense along a gently W-dipping extensional shear zone or detachment. Measurements initially taken in the Steels Pass area were subsequently observed further north on Brazil Ridge leading to the conclusion that this zone of dextral shear extends north-northeast from Steels Pass. Further investigation to the south of Steels Pass would likely confirm the southern extension of the Steels Pass shear zone.

The Steels Pass shear zone is thought to be a line of detachment along which the Highlands Mountains gneiss dome was exhumed. This hypothesis is supported by clast

15

kinematics observed in the leucogranites of the shear zone and the geometry of the gneiss dome itself. Down-to-the-west shear along the Steels Pass shear zone would accommodate the exhumation of the gneiss dome as seen to the east and south of Steels Pass (Figure 31). The Steels Pass shear zone is truncated in the north and south by the Cretaceous Hell Canyon Pluton and the reactivated Tertiary Twin Bridges Fault, respectively (O'Neill et al., 1988).

Domain 2 transitions south into domain 3 across Steels Pass Creek. Domain 3 is defined by the prevalence of parasitic folds formed on the limbs of a sub-horizontal, upright antiform. Field measurements indicate that the foliations in domain 3 steepen upwards towards the axial surface of the antiform. Leucogranite and mafic sills are abundant though they are not consistently oriented along the fabric of domain 3 as they are in domain 2. The antiform structure may be part of a second-order fold complex comprising the westernmost structural exposure of the Highlands Mountains gneiss dome.

Deformation Setting

The suite of microstructures observed in thin section indicate deformation associated with the exhumation of the Highland Mountains gneiss dome ceased while the involved rocks were still at significant depth in the presence of hydrothermal fluids.

Microstructures indicate two phases of deformation: the first being syn-tectonic (structures formed during the tectonic deformation event that drove the metamorphism) and the second being post-tectonic (structures formed after the tectonic deformation has ceased). Syn-tectonic conditions for these rocks are characterized by lower amphibolite facies metamorphism, not exceeding 600˚C, based on quartz and feldspar microstructures (Tullis, 2002). Under these conditions, garnet may have grown in the migmatite sill (MT11-01) and the quartz + feldspar +

biotite gneiss of domain 1 (12B-15B). Along the Steels Pass shear zone in domain 2,

leucogranite sills (12B-01 and 12B-46B) were emplaced under syn-tectonic conditions, i.e., the

deforming shear motion influences the shape and orientation of the quartz ribbons and clasts

during emplacement, indicating a shallow-west-dipping dextral sense of shear (evidence of this

shear is seen both in outcrop and in thin section; Figures 14, 17, 22, and 24). The deformed syn-

kinematic clasts of plagioclase underwent a dynamic recrystallization process, forming core-

mantle structures, which lower the total internal energy configuration of the clast (Figure 23).

Syn-tectonic deformation ceased at relatively high temperatures in the presence of some amount

of melt and/or grain boundary/pore fluids. The post-tectonic processes of static recrystallization

subsequently dominated apparently while the terrain was cooling and being exhumed. During

static recrystallizaton, sub-grain boundaries are developed in the quartz ribbons and clasts as the

dislocations are swept to zones of higher concentration (Evans et al., 2001; Paschier and Trouw,

2005). Dislocation tangles are removed as the grain boundaries tend to grow and straighten

while undergoing GBAR (grain boundary area reduction) (Paschier and Trouw, 2005). The

grains themselves become more polygonal in form (foam texture) as a result of the GBAR

(Figure 32).

Monazite Geochronology

The monazite geochronology study sought to establish the timing of the Highland

Mountains gneiss dome with respect to the emplacement of a local leucogranite sill complex.

Understanding this relationship would allow important constraints to be placed on the timing and

deformation of the Highland Mountains gneiss dome with respect to the development of the

GFTZ and the Steels Pass shear zone.

Emplacement of the sill complex was initially defined by Mueller et al. (2005) based on ca. 1.77 Ga crystallization ages for one leucogranite from the area. Sample 12B-46B did not preserve any evidence for ca. 1.77 Ga monazite, but did contain abundant inherited ~2.5 Ga (Archean) monazites (P1). Leucogranite sill 12B-46B apparently did not grow monazite during emplacement due to its bulk composition and/or pressure-temperature-fluid constraints. Monazite growth requires a phosphatic (PO_4) bulk composition containing rare earth elements (REE's) such as Cerium and Yttrium (Williams et al., 2006a). The leucogranite sill 12B-46B did inherit at least four Archean monazite grains from the surrounding country rock (X(A)qf). Some 200 My later, a Mesoproterozoic passive intracontinental rifting event caused by lithospheric extension led to the formation of the Belt-Purcell basin (Chandler, 2000). This rifting event is inferred to coincide with the growth of the younger monazite population (P2). This passive rifting event drove extensional faulting and sporadic tholeitic to alkaline magmatism to occur in the period of ~1500 Ma to about 1320 Ma during deposition of the Belt supergroup (Lydon, 2008). The intracontinental rifting and associated magmatism could have mobilized reactive Th, Si, Ca, and (Y + REE) grain boundary/pore fluids into communication with the sill complex leucogranites, causing grain alteration and growing ca. 1.5 Ga (P2) Mesoproterozoic rims on the inherited Archean monazite cores (M1, M5, and M7; Figures 29 and 30) (e.g. Bingen and van Breemen, 1998; Hansen and Harlov, 2007; Rasmussen and Muhling, 2007; Simmat and Raith, 2008; Martins et al., 2009; Harlov et al., 2010).

VII. Conclusions

This research has examined the timing and deformation of the Highland Mountains gneiss dome by focusing on a local leucogranite sill complex as situated within the

Great Falls tectonic zone. The following represents a preferred order of events.

Circa 2.5 Ga*:* Monazite grains form and record the crystallization ages of either and/or both of the separate Archean Medicine Hat block and Wyoming Province terranes.

1.78 – 1.72 Ga: The GFTZ closes along its NE-SW trend driving orogenesis and significant crustal thickening (Harms et al, 2006). Leucogranite sill emplacement at depth along the Steels Pass shear zone coincides with extension caused with post-orogenic crustal thinning. The crustal extension and associated top-down-to-the-west shear along the Steels Pass shear zone allow the development of the Highland Mountains gneiss dome. All leucogranite sills emplaced during this extension contain monazite (P1) inherited from the Archean country rock and some sills (constrained by their bulk composition) include new monazite grains that formed during the time of leucogranite crystallization. The sill sampled in this study apparently did not have the appropriate bulk composition to grow monazite at 1.78-1.72 Ga, if it was emplaced at this time (as dated for a different leucogranite sill nearby by Mueller et al. (2005). Core-mantle micro-structures developed in the leucogranites as a result of syn-tectonic dynamic recrystallization. Following the crustal extension and syn-tectonic deformation, post-tectonic deformation processes dominated. This results in the static recrystallization processes of GBAR and develops the foam-like grain texture seen in thin section.

Circa 1.5 Ga: The Belt-Purcell passive intracontinental rifting event mobilized enriched (Y+REE) hydrothermal grain boundary/pore fluids from the alkaline/tholeitic melts into communication with the local leucogranite sill complex. Presence of the enriched fluids drove monazite grain alteration and grew a younger population (P2) of high-Y monazite rims on the old (P1) Archean monazite cores. Monazite grains are individually altered by variations in the enriched fluid composition and reaction conditions.

Today: Two populations of monazite grains are seen (P1 ~2.5 Ga and P2 ~1.5 Ga) in leucogranite sill 12B-46B. Neither of these populations may represent the actual crystallization age of this individual sill. The annealed textures of the thin section micro-structures may represent the combination of effects of the syn- and post-tectonic deformation processes as well as the reactions and alterations that took place during the growth of the younger monazite population (P2).

VIII. Figures

Figures 1A and 1B:

Figure 1A) A regional location map showing the Highlands Mountains situated within the Great Falls tectonic zone (O'Neill and Lopez, 1985), between the Wyoming craton to the southeast and the Medicine Hat block to the northwest. Adapted from Ault et al. (2012)

Figure 1B) Foliation trajectory contour map drawn from the field data of O'Neill et al. (1996), illustrating simplified local geology along with foliation trajectory contours defining the structural gneiss dome as well as a central NE-SW doubly-plunging antiform.

Figure 2:
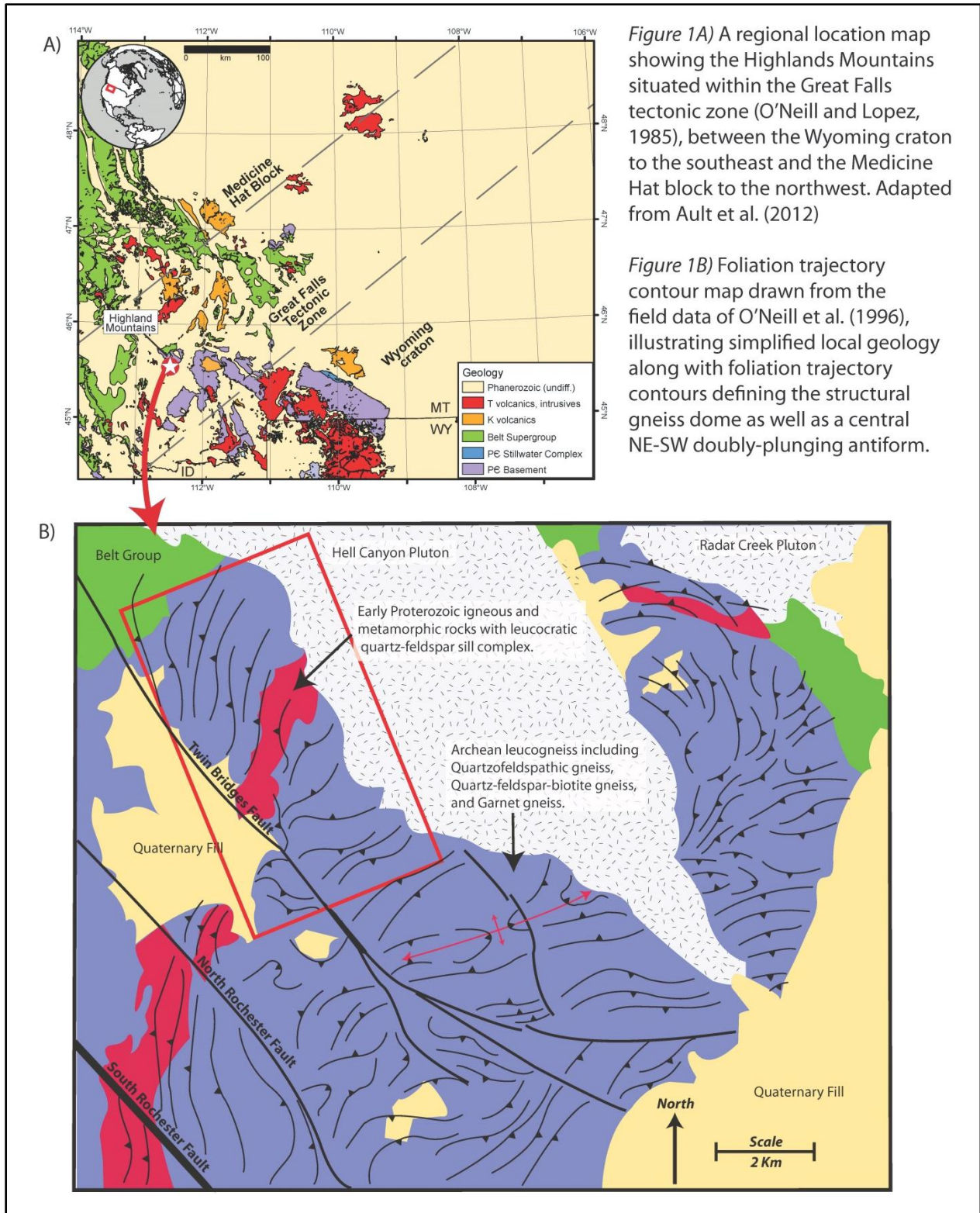
Adapted from O'Neill and Lopez (1985), this figure illustrates the extent of the Great Falls tectonic zone and other related geologic features at the scale of North America.

(O'Neill and Lopez, 1985)

Figure 3:

Adapted from Mueller et al. (2005), this figure illustrates the position of the Great Falls tectonic zone relative to the associated regional geologic provinces and orogenic zones.
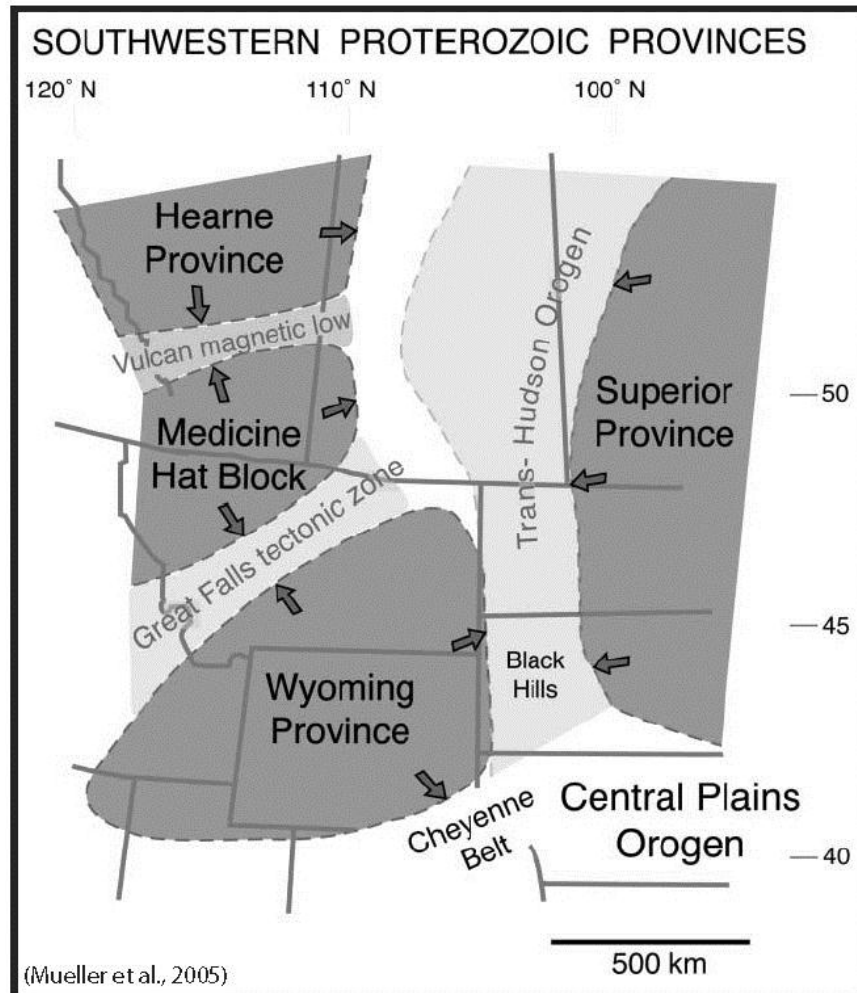
Figure 4:

Geologic map and data resulting from field investigation. Base layer topography adapted from USGS Table Mountain, MT Quadrangle. Cross section A-A' is depicted in Figure 6.
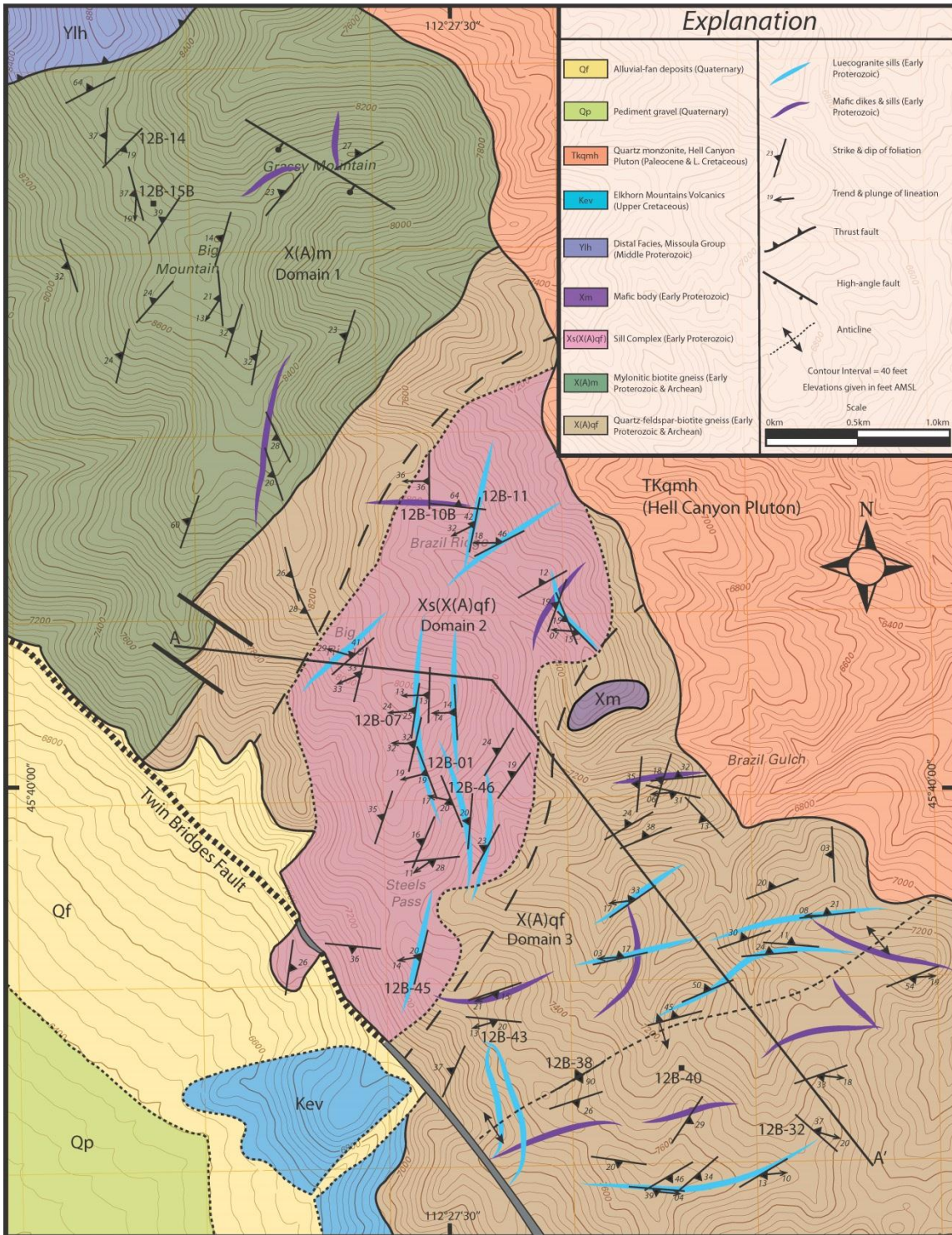
Figure 5:

    Contoured foliation measurements illustrating changes in fabric orientation across the field area.
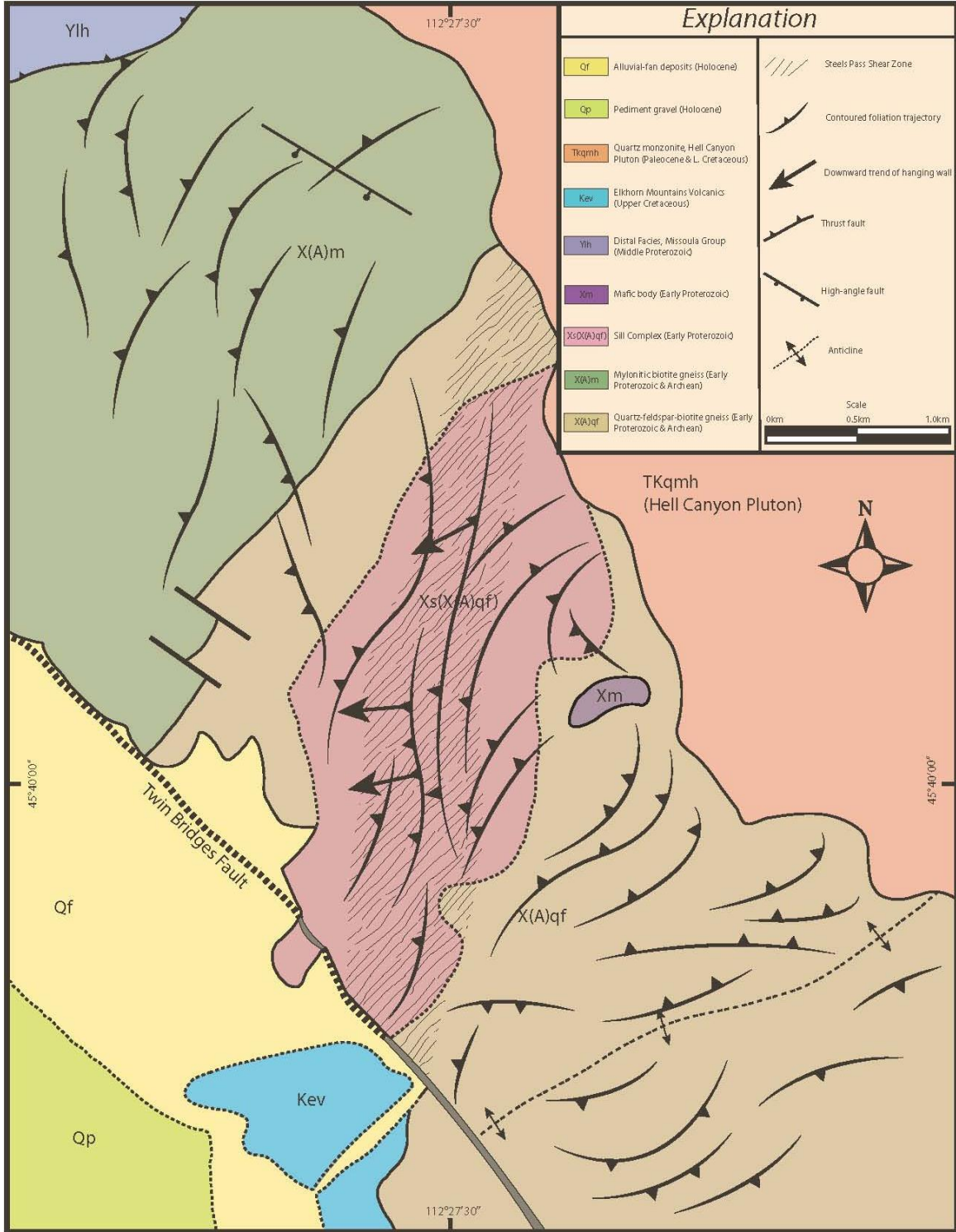
Figure 6:   Cross section and lower hemisphere equal area stereonets illustrating variations in elevation, lithology, structure and fabric orientation across the field area. Note domain 1 continues NW from end of section.
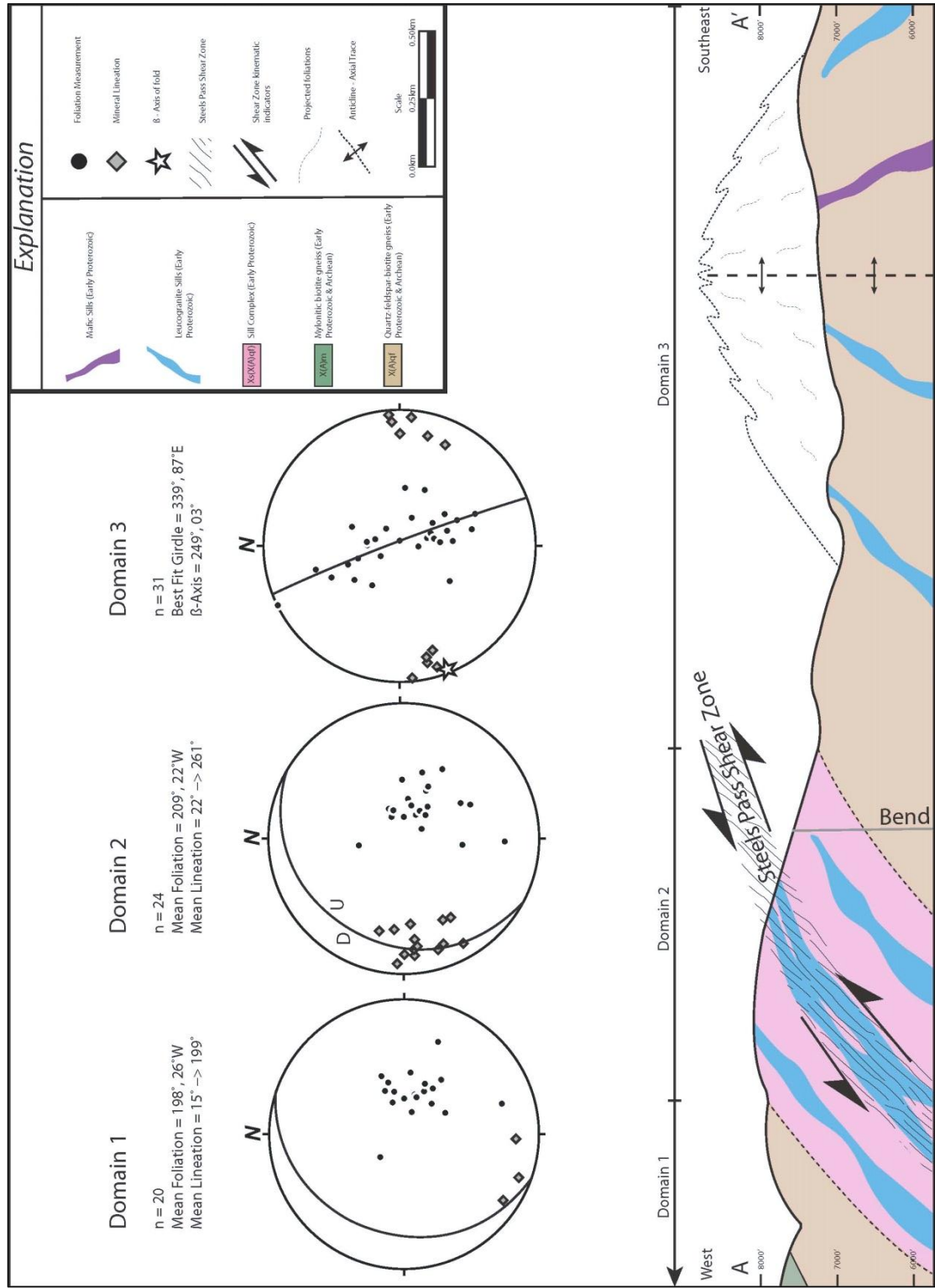
Figure 7:
    Full section Ca Kα map of thin section 12b-46b. Inset Y Lα and Th Mα maps of each individual monazite grain. Brighter colors indicate higher element concentration.

27

Figure 8:
Full section Ca Kα map of thin section 12b-15b. Inset Y Lα and Th Mα maps of each individual monazite grain. Brighter colors indicate higher element concentration.

Figure 9:
    Full section Ca Kα map of thin section MT11-01. Inset Y Lα and Th Mα maps of each individual monazite grain. Brighter colors indicate higher element concentration.
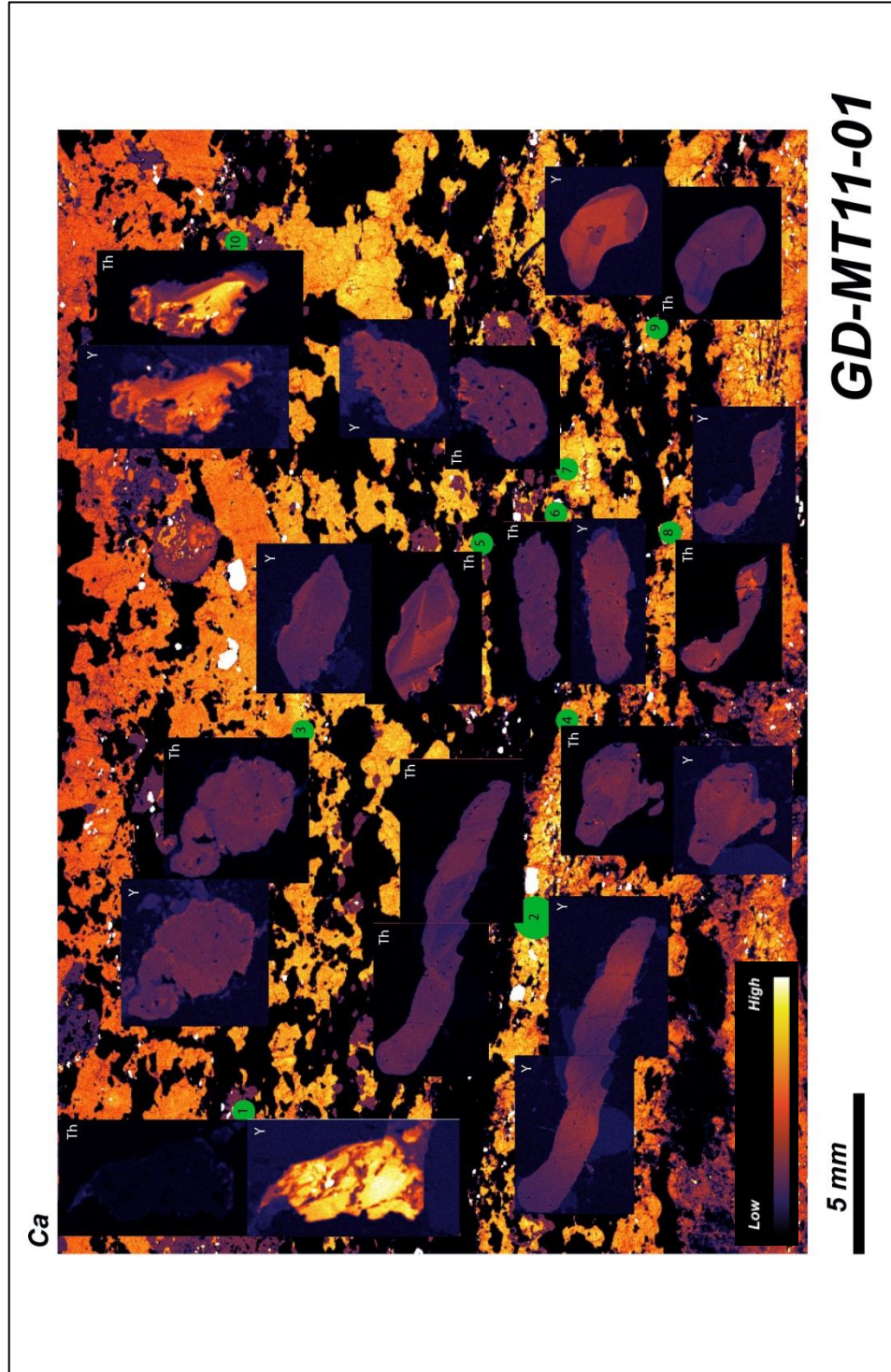
Figure 10:
        Average dates plotted for each sample domain. Two populations are apparent, population 1 (P1) has an average date of 2444.87 ± 392 Ma, and population 2 (P2) has an average date of 1534.27 ± 116 Ma. Error bars represent the ±2σ standard deviation for each population. Complete monazite dataset is seen in Table 1A-1D.
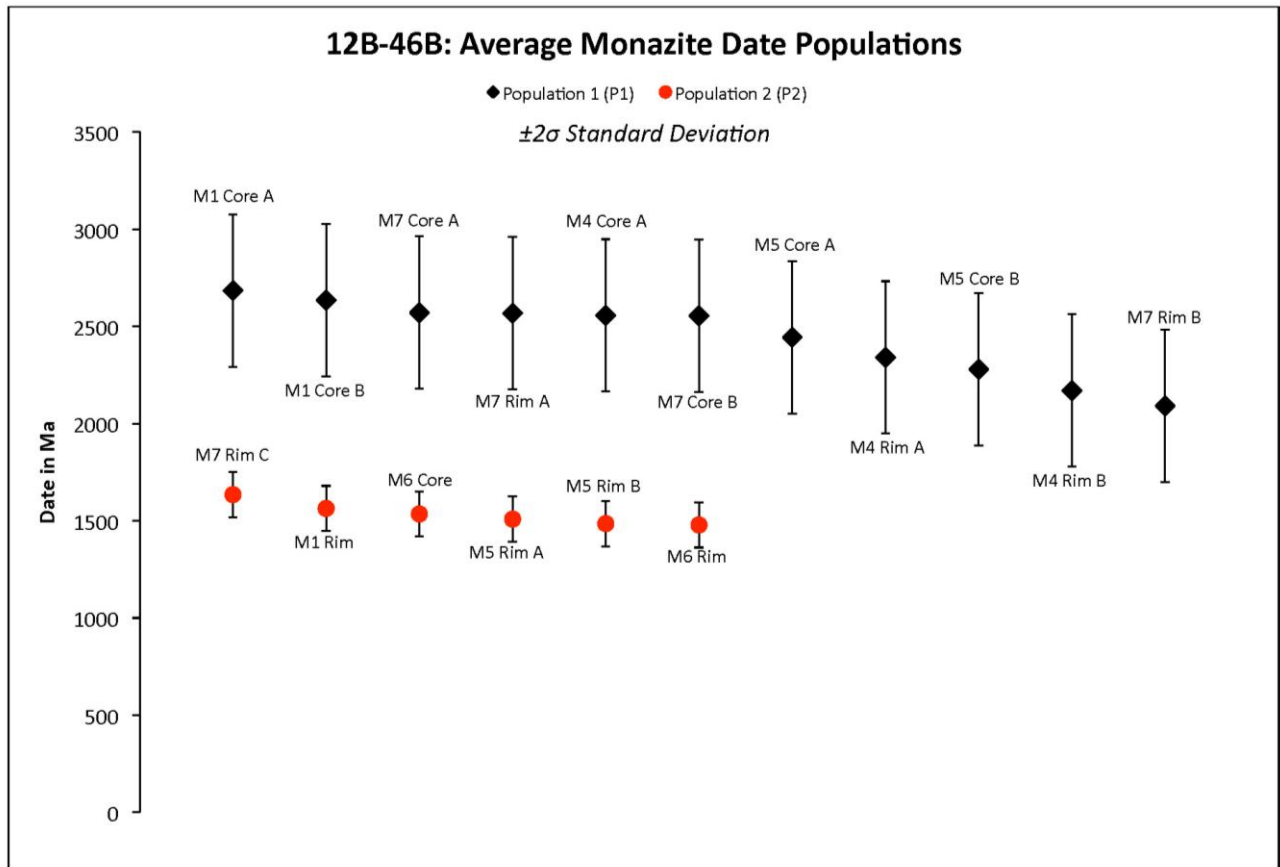
Figure 11:
    Monazite date count histogram. Each bar represents the number of dates calculated within that corresponding 100 My age bin. The red curve illustrates a polynomial fit to the data. The two peaks seen at ~ 1.5 and ~ 2.5 Ga represent the dominant monazite date populations P2 and P1 respectively.
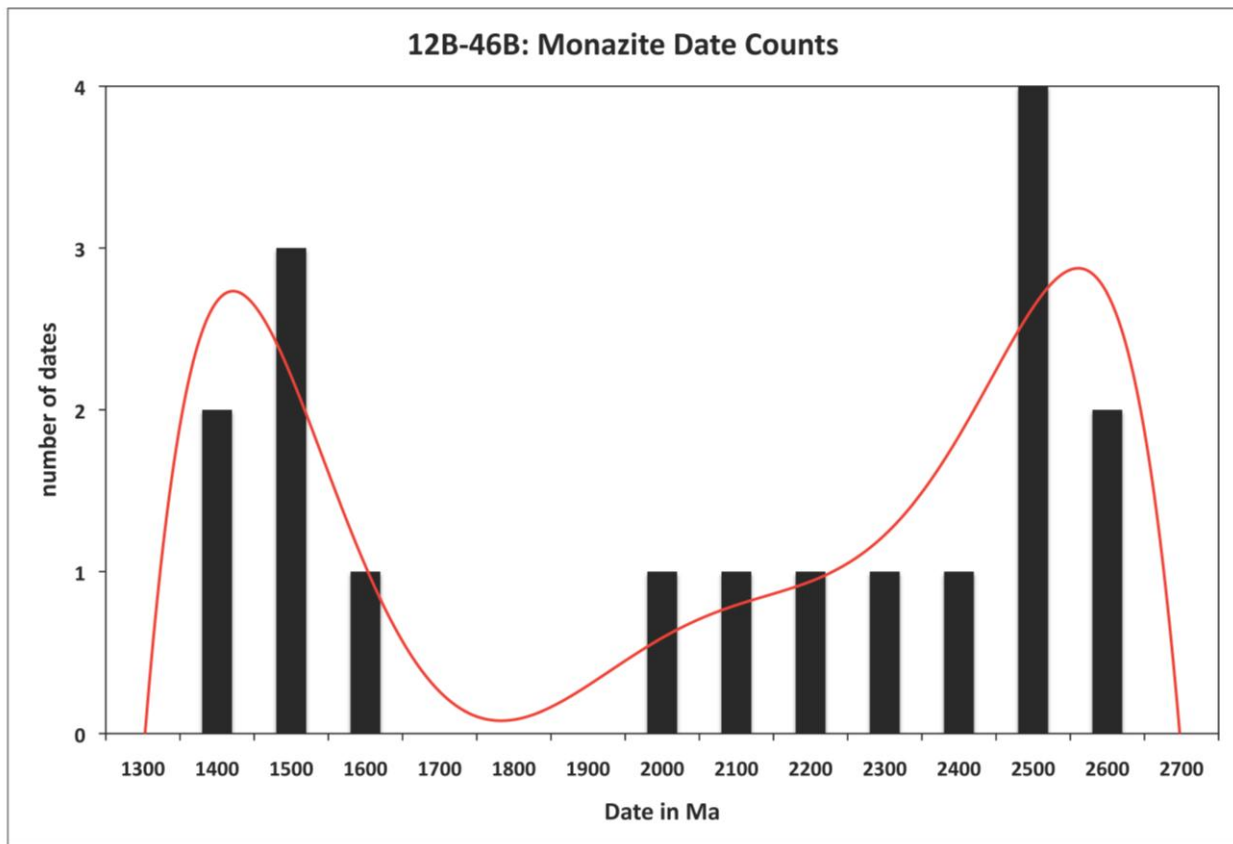
Figure 12:
    This field image taken at site 12B-14 (See Figure 4 for location) illustrates the textures and mineralogy seen in the Archean Mylonitic gneiss (X(A)m) of domain 1. This location in particular is abundant with garnet retrogressed to biotite. U.S. quarter for scale. Photo Credit: Lane Boyer, August 2012.

12B - 14

X(A)m - Garnet laden, biotite gneiss.
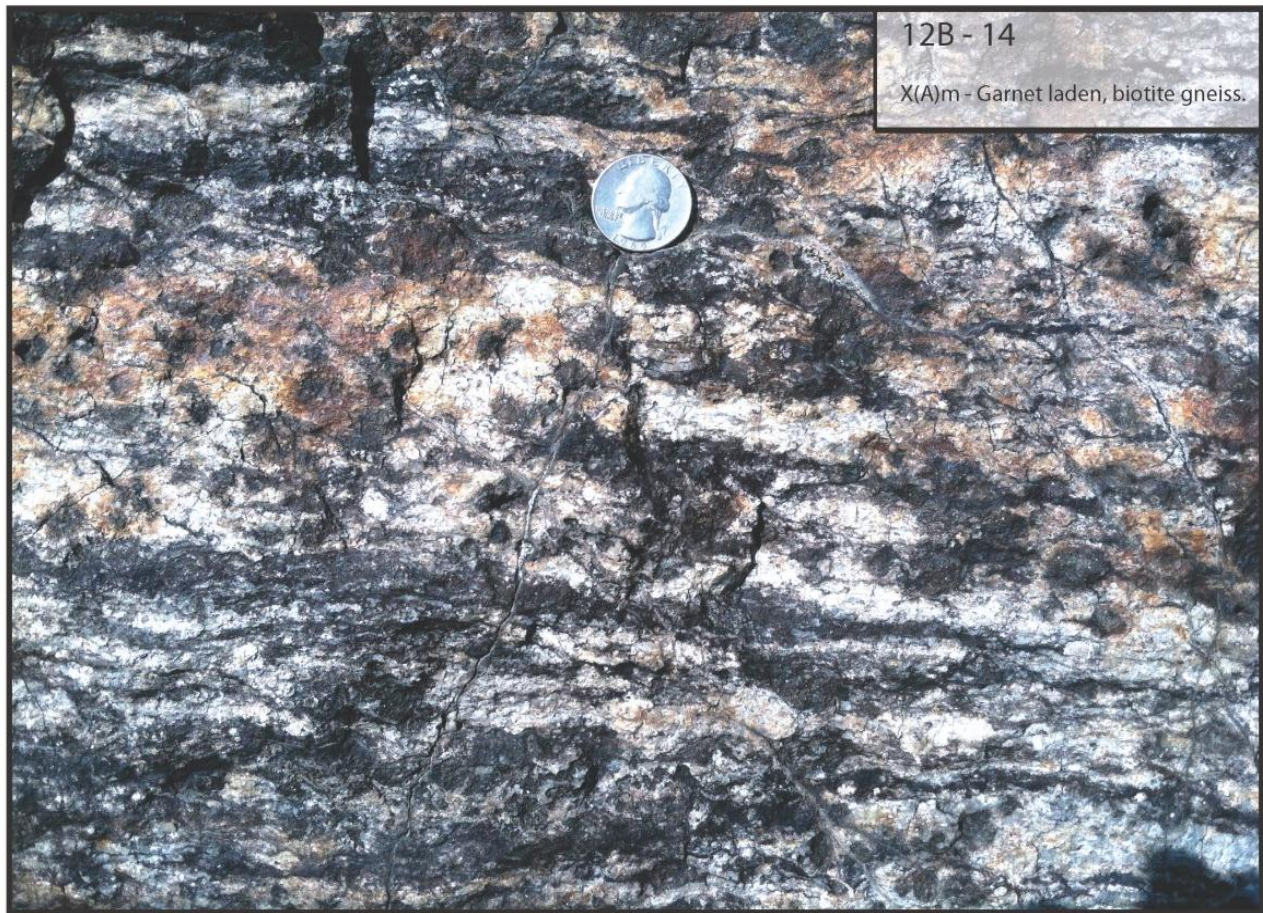
Figure 13:
        This outcrop image at site 12B-15B illustrates a kinematic garnet δ – clast with leucocratic tails indicating a top-down-to-the-west-southwest shear sense. Pencil tip for scale. Photo Credit: Greg Dumond, August 2012.
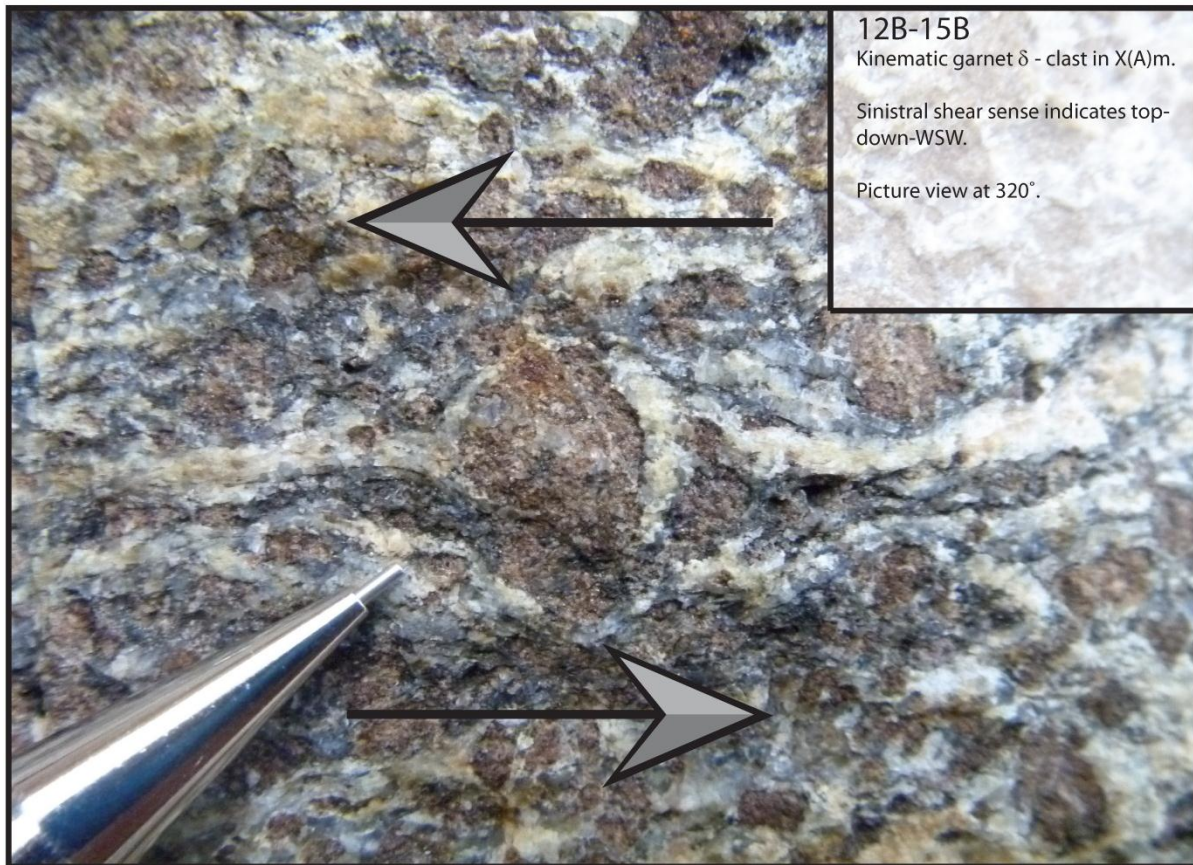
Figure 14:

        Field shot taken at site 12B-01 just north of Steels Pass, within the Steels Pass shear zone. The shear zone fabric strikes at ~160° and has a shallow dip to the west-southwest at ~20° defined by leucogranite sills and porphyclasts of plagioclase and k-feldspar with quartz ribbons (See inset image). The author for scale. Photo Credit: Greg Dumond, August 2012.

12B - 01
Shallow WSW dipping Steels Pass
shear zone. (160˚, 20˚SW)
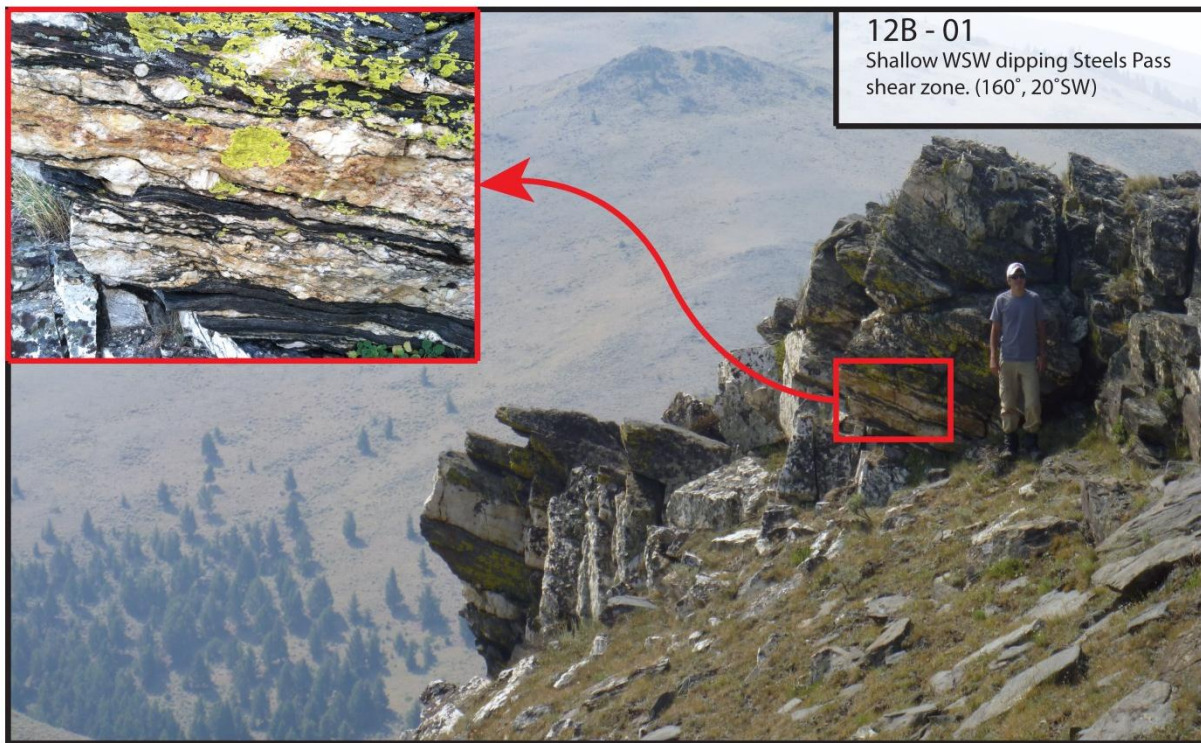
Figure 15:

        Outcrop at site 12B-46, within the Steels Pass shear zone, exposing the leucogranite sills. Fabric is defined by the leucocratic layers, leucogranite sills and biotite in the host gneiss. Hammer for scale. Photo Credit: Lane Boyer, August 2012.

12B - 46

Leucogranite sills intruding mafic host rocks in the Steels Pass shear zone.

Fabric: 153˚, 20˚SW

Viewing at 250˚.

Figure 16:

Field image taken at site 12B-07 within the Steels Pass shear zone. This figure illustrates a plagioclase σ-clast with sinistral top-down-to-the-west-southwest shear. Fabric is defined by quartz ribbons and deformed plagioclase clasts. U.S. quarter for scale. Photo Credit: Greg Dumond, August 2012.
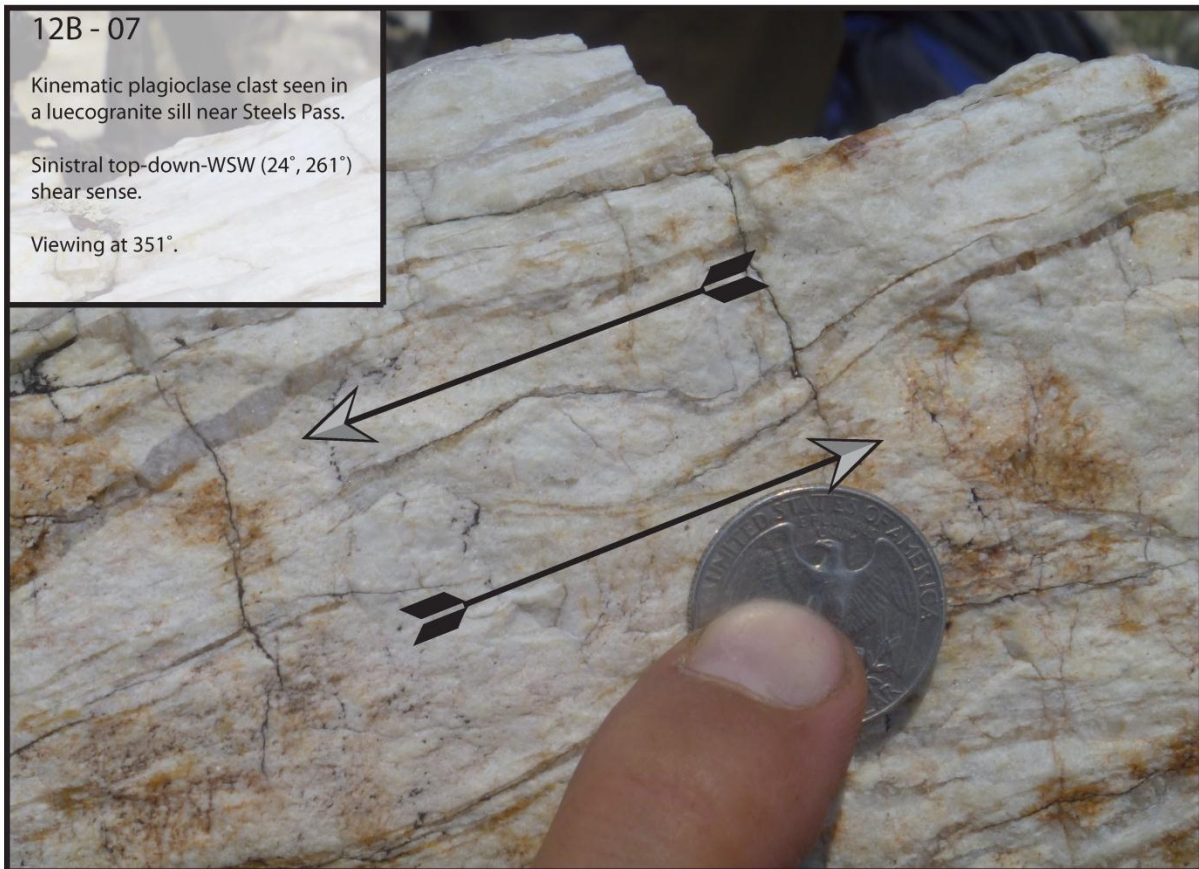
Figure 17:

Outcrop at site 12B-46, within the Steels Pass shear zone, seen here is a ~2 meter thick leucogranite sill fully exposed in outcrop. The base of this sill was heavily corrugated with a lineation at 17°→250°, indicating syn- to post-emplacement deformation of the sill along the shear zone fabric. This is the sill analyzed in the monazite geochronology study. Hammer for scale. Photo Credit: Lane Boyer, August 2012.
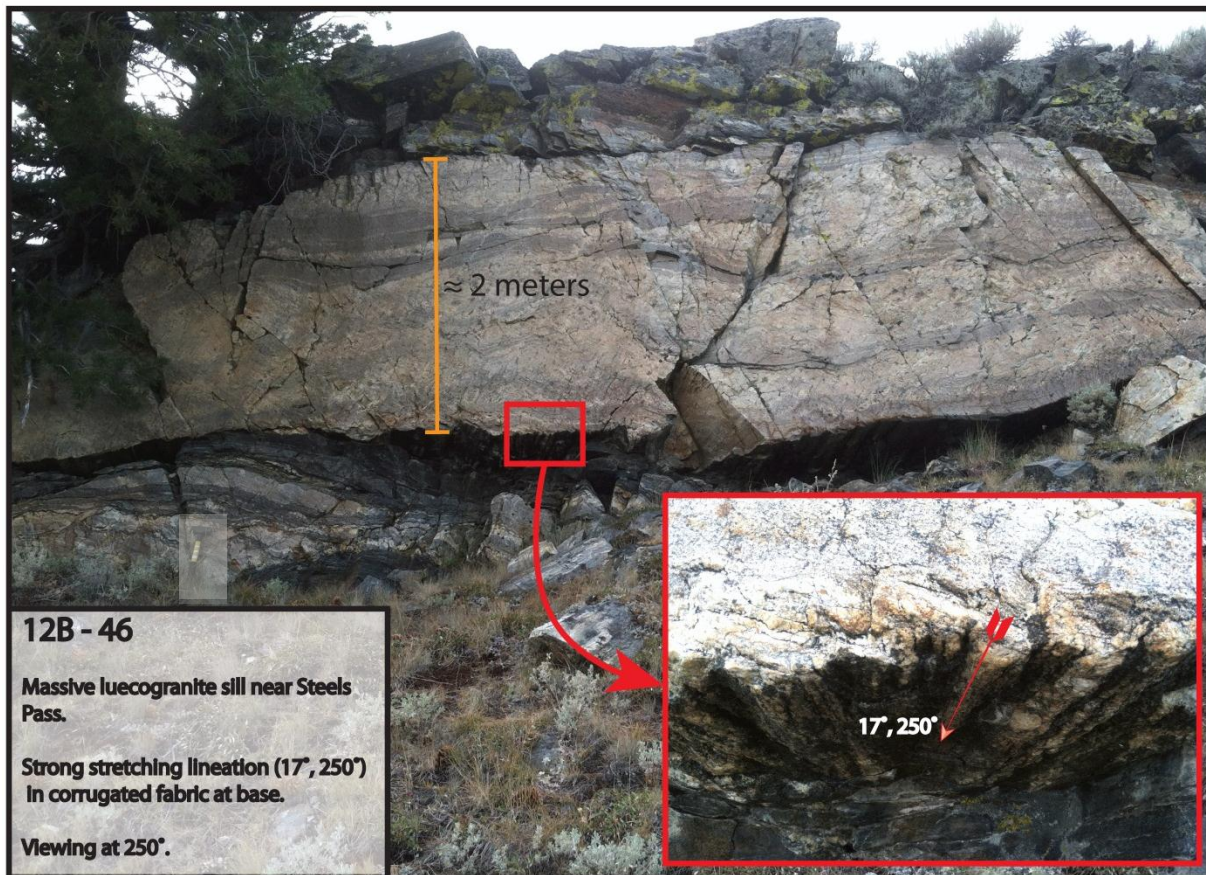
Figure 18:

      This field shot taken at site 12B-11 on Brazil Ridge illustrates the northern continuation of the Steels Pass shear zone. The plagioclase σ-clast seen here indicates a top-down-to-the-west-southwest shear sense, plunging at 32° towards 246°. Pen for scale. Photo Credit: Greg Dumond, August 2012.

12B - 11

Kinematic plagioclase clast seen in a luecogranite sill on Brazil Ridge.

Sinistral top-down-WSW (32°, 246°) shear sense. Viewing at 336°.

Figure 19:

        Outcrop at site 12B-43 on the western limb of the antiform mapped in domain 3. The fabric is defined here by granite pegmatic layers within the quartz+feldspar+biotite gneiss (X(A)qf) (See inset image). The parasitic folds seen here steepen to the east as one approaches the hinge of the anitform. Hammer for scale. Photo Credit: Lane Boyer, August 2012.
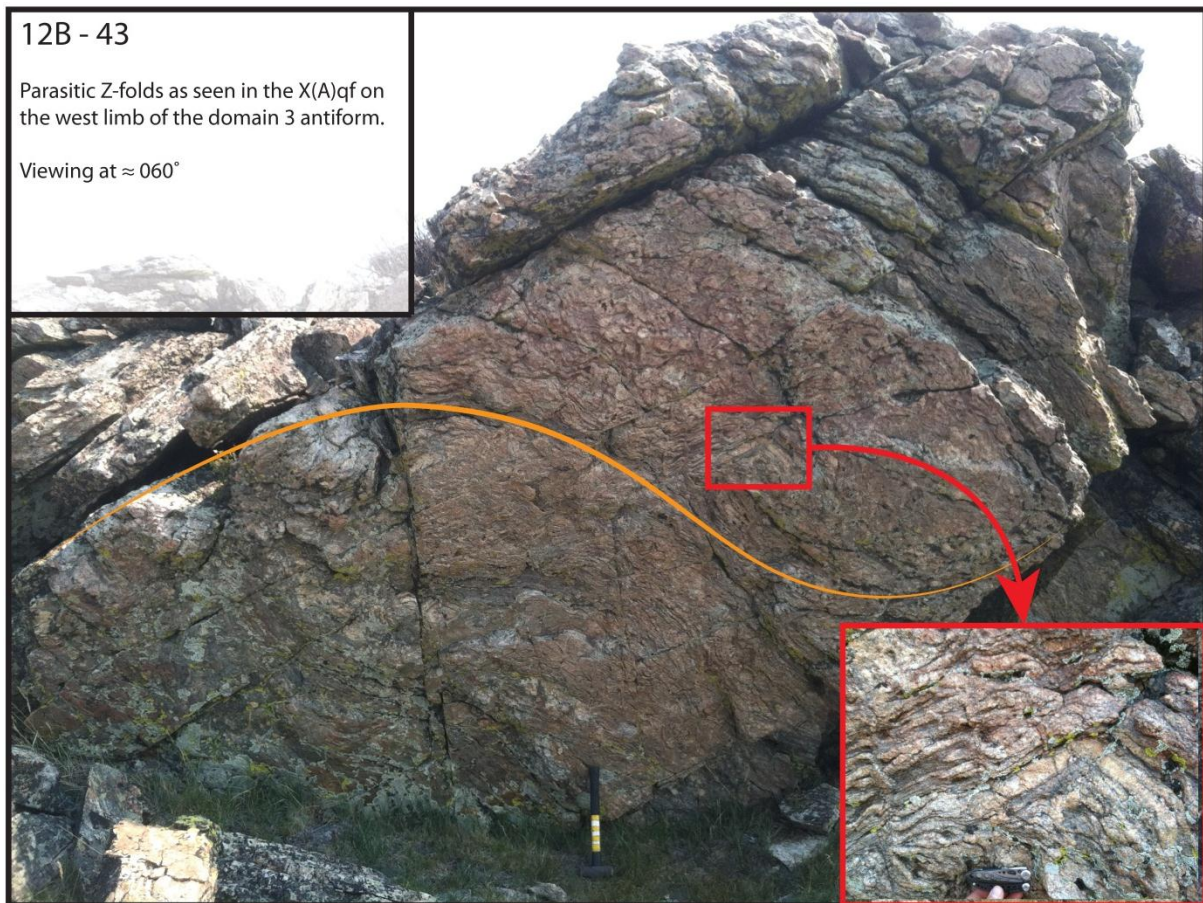
Figure 20:

Outcrop at site 12B-38 illustrates the near vertical fabric in X(A)qf seen near the hinge of the domain 3 antiform. The steep S1 fabric (yellow) is overprinted by the shallow S2 fabric (red). This shallow S2 fabric may relate to the formation of the Highland Mountains gneiss dome. Pencil for scale. Photo Credit: Lane Boyer, August 2012.
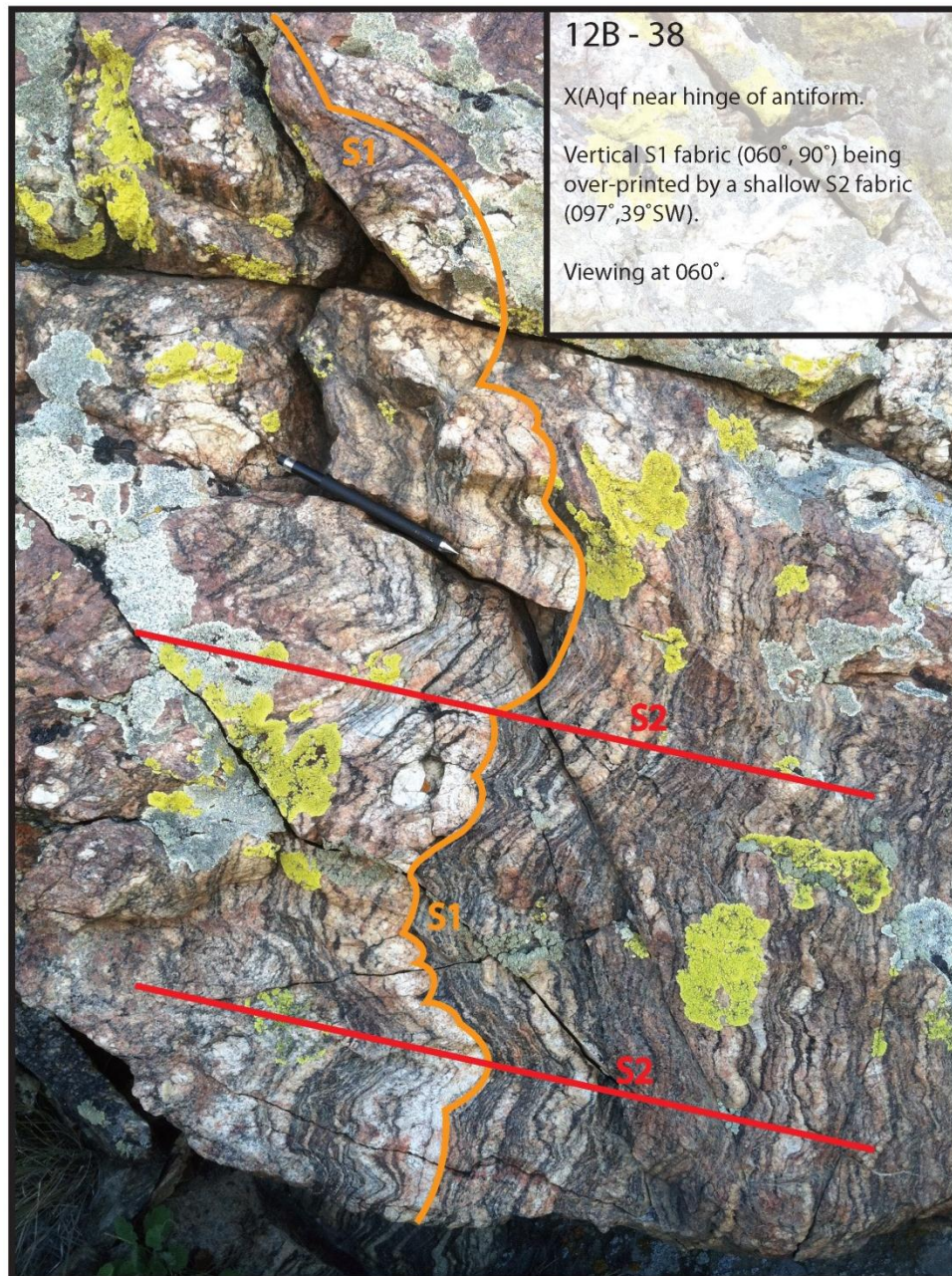
Figure 21:
Full section scan of X(A)m in thin section from site 12B-15B. Inset cross-polarized microscope images (A – the rock matrix of k-fels + plag + qtz + bt + grt; B – a deformed garnet porphryobalst; and C – a well-developed qtz ribbon) illustrate the variety of microstructures seen in this sample. Thin-section ~ 45mm in length.

12B - 15B

X(A)m in Thin Section

A: Kfels + Plag + Qtz + Bt + Grt
B: Oblate fractured Grt in replacement by Bt.
C: Ribbon Qtz with Bt.

41
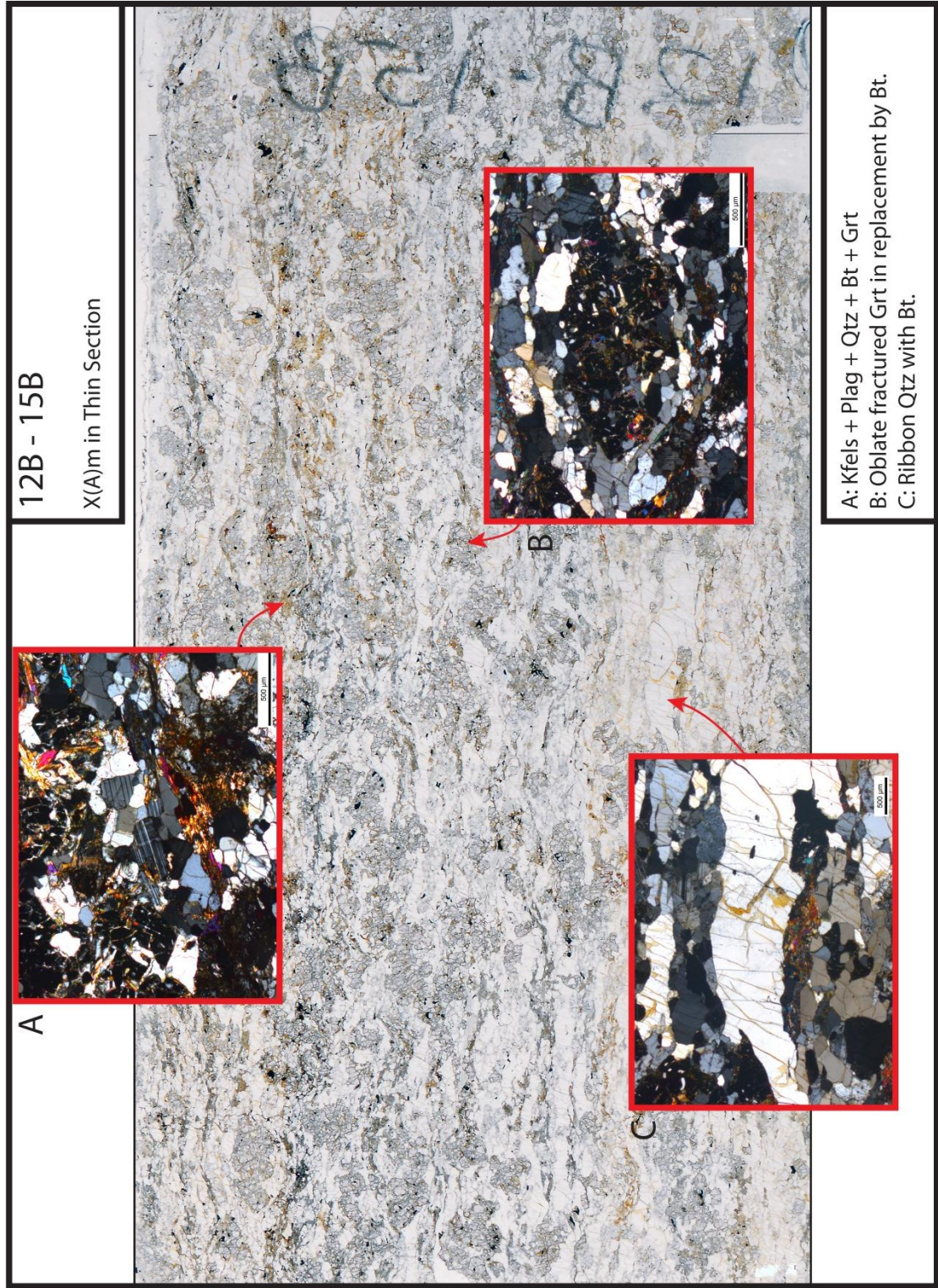
Figure 22:
    Full section scan of a leucogranite sill in thin section from site 12B-01. Inset cross-polarized microscope image illustrates the development of core-mantle structure around the larger clasts of plagioclase. Pl = Plagioclase. Thin-section ~ 45mm in length.
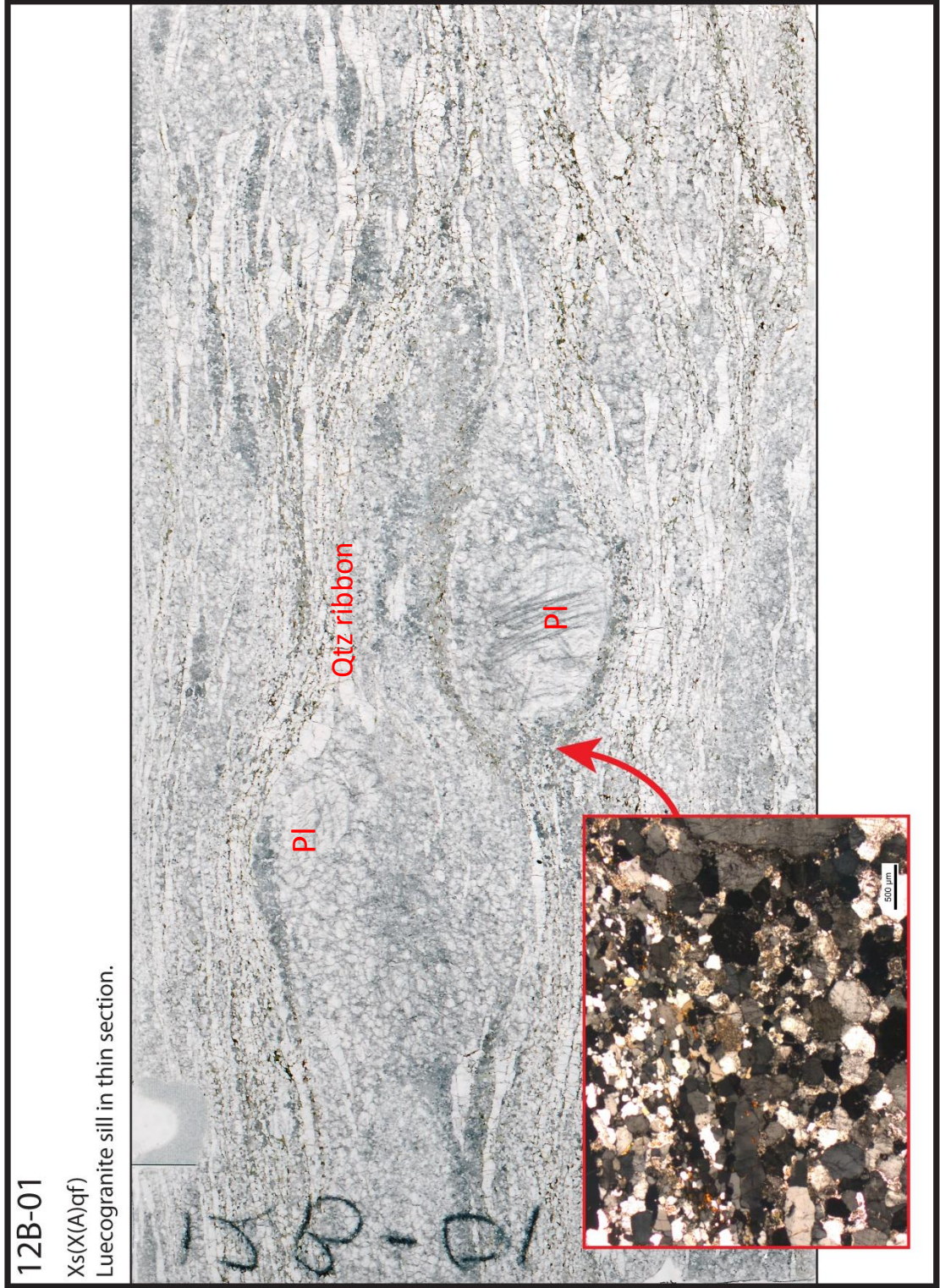
Figure 23:
Full section scan of a leucogranite sill in thin section from site 12B-11 on Brazil Ridge. Inset cross-polarized microscope image illustrates the development of core-mantle structure and undulose extinction in the remnant core clast. Thin-section ~ 45mm in length.

12B-11
Luecogranite sill Xs(X(A)qf) in thin section.
Sampled on Brazil Ridge
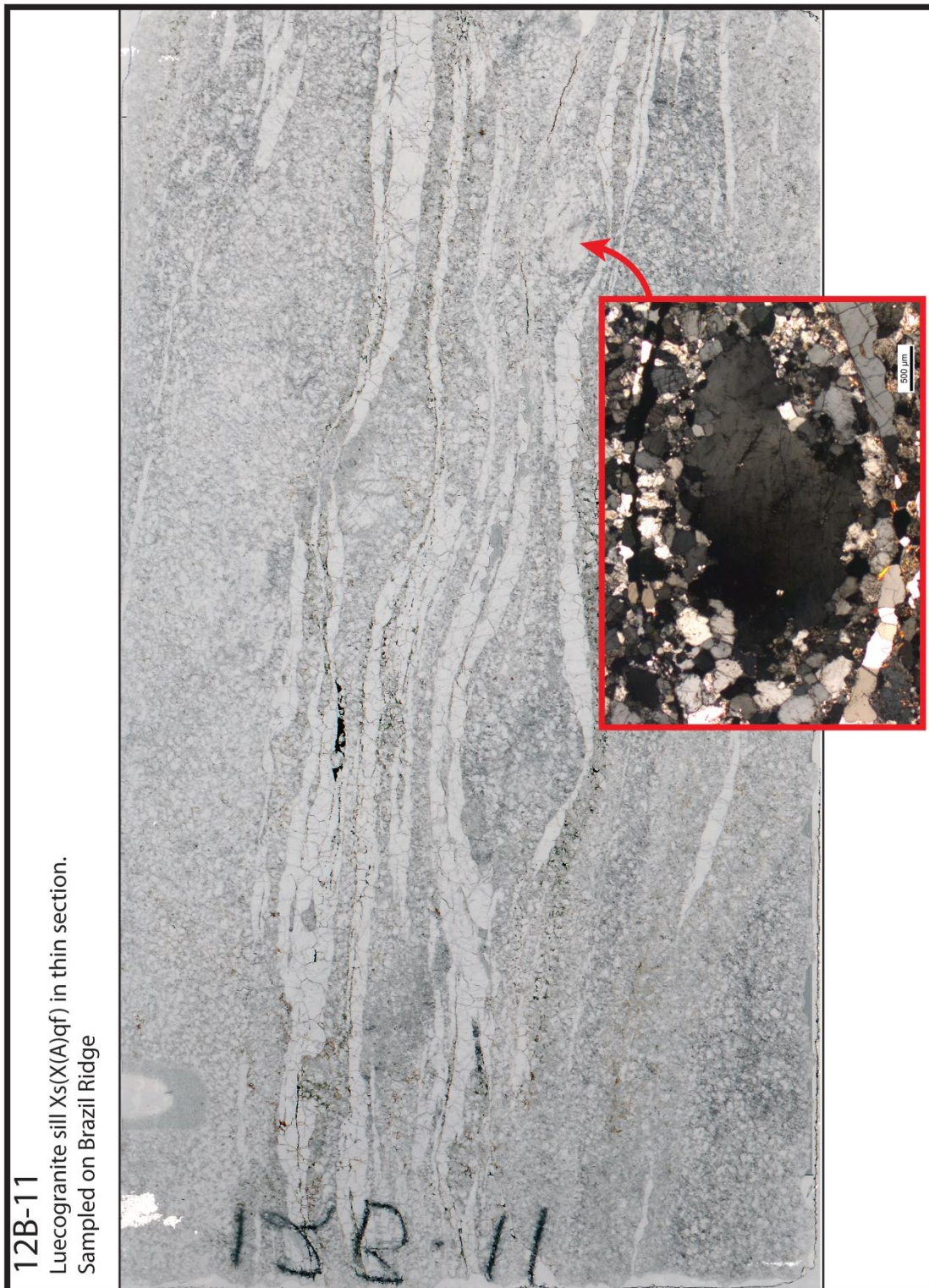
Figure 24:

Full section scan of leucogranite sill sample 12B-46B within the Steels Pass shear zone. Inset cross-polarized microscope image illustrates core-mantle structure and undulose extinction in the neighboring quartz ribbon as it is deformed adjacent to the remnant core plagioclase clast. Thin-section is ~ 45mm in length.

12B-46B

Fine-grained luecogranite sill Xs(X(A)qf) in thin section.
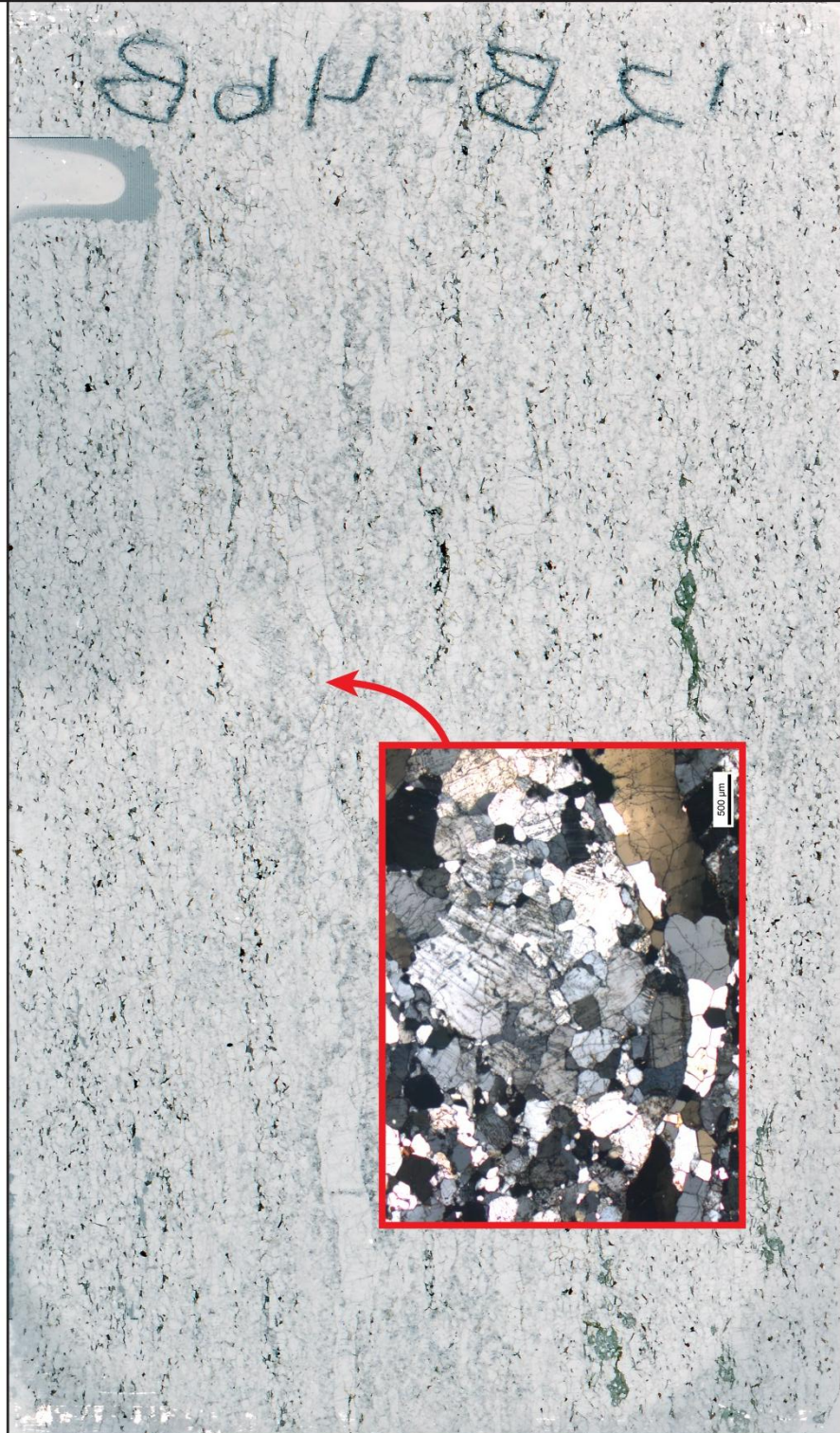
Figure 25:
    Full section scan of mafic granulite (Xm) sill sample 12B-10B from Brazil Ridge. Inset cross-polarized microscope image illustrates remnant garnet in replacement by biotite and surrounded by a fine-grained matrix of mafic minerals such as hornblende and augite. Thin-section is ~ 45mm in length.

12B - 10B
Mafic granulite sill (Xm) in thin section
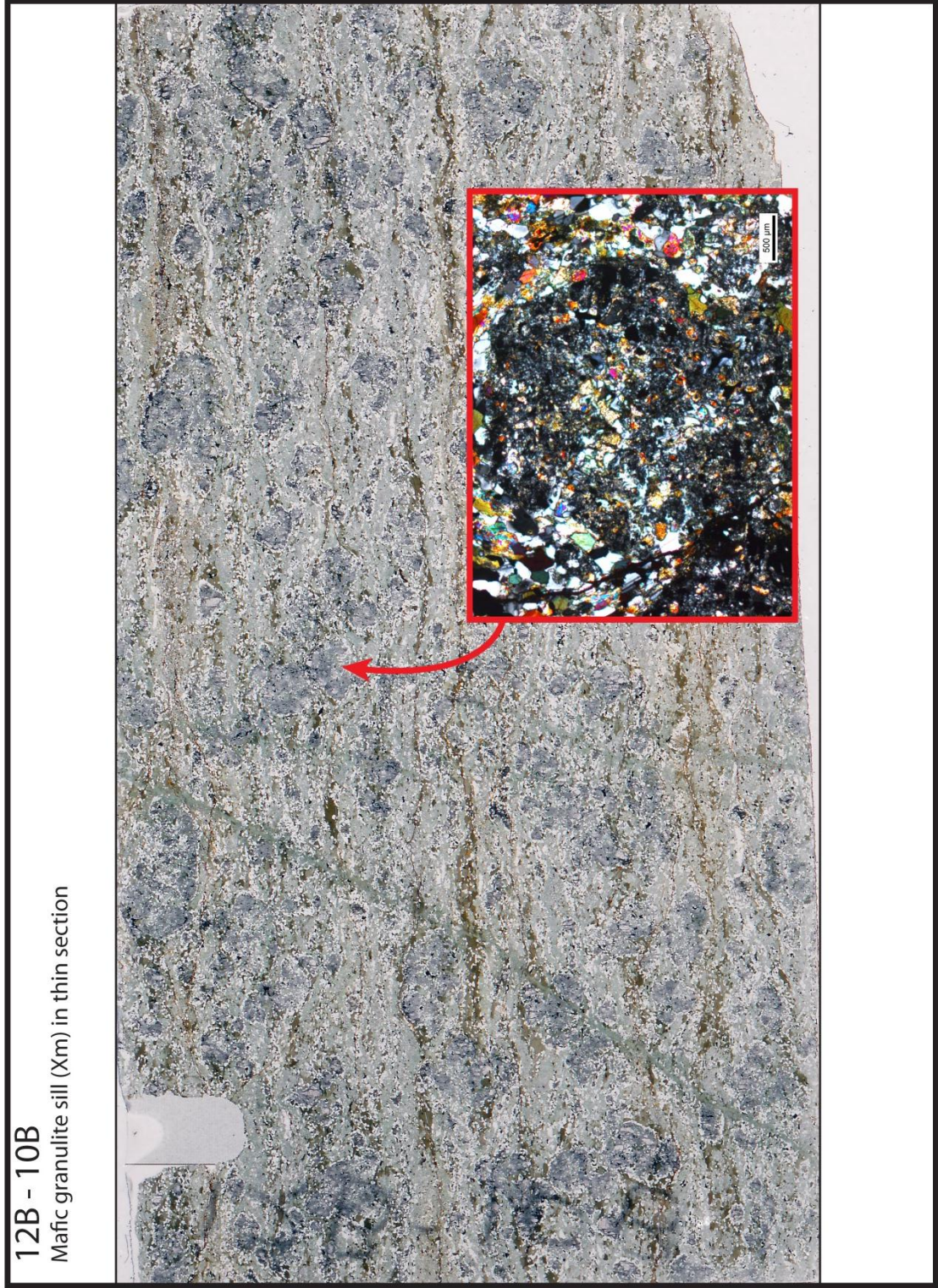
Figure 26:

Full section scan of leucogranite sill sample 12B-32 from the east limb of the domain 3 anitform. This scan illustrates the coarse grained nature of this sill . Thin-section is ~ 45mm in length.

12B-32

Luecogranite sill Xs(X(A)qf) in thin section.
Large kinematic plagioclase.
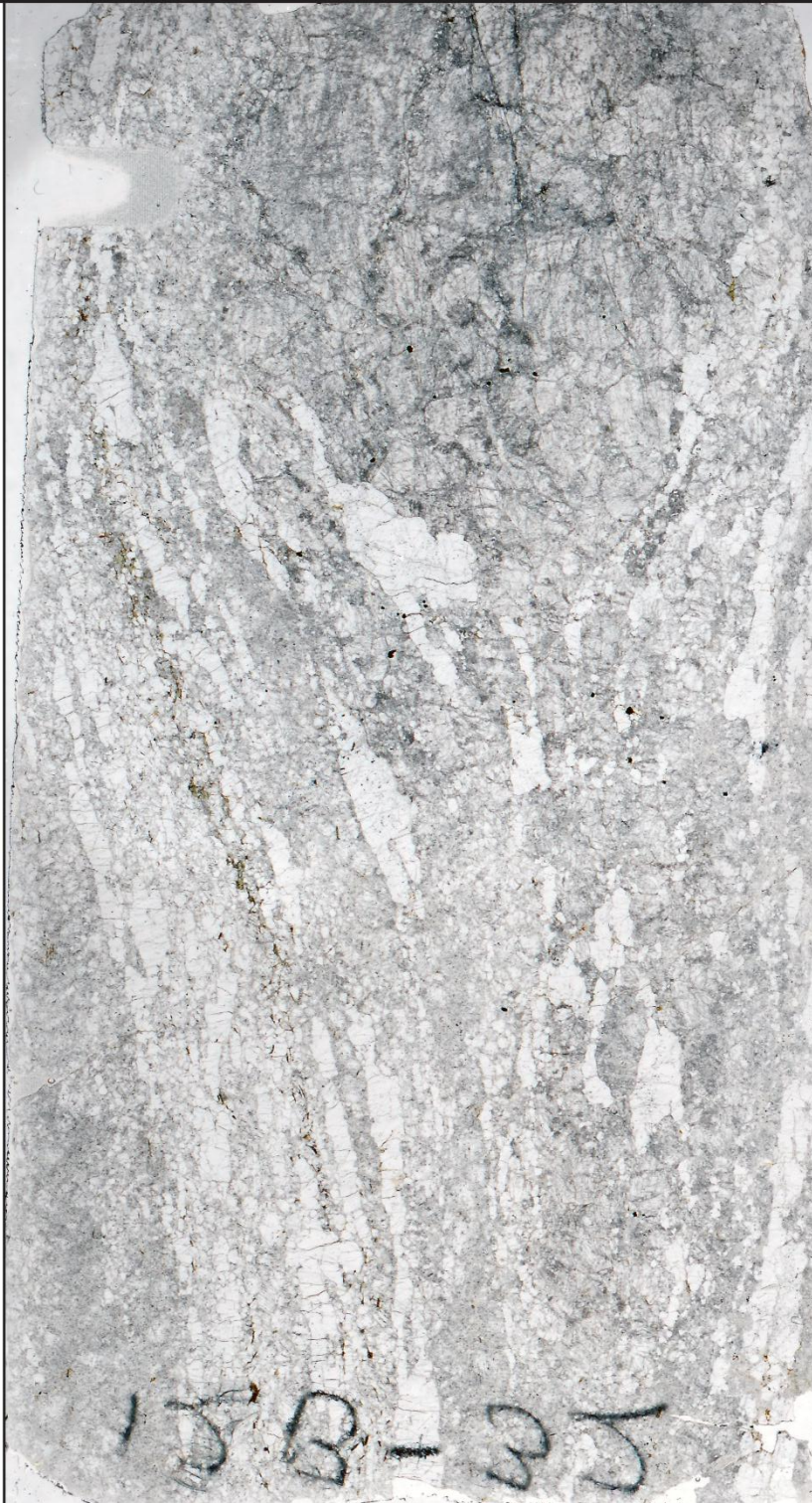
Figure 27:
    Full section scan of leucogranite sill sample 12B-40 from the west limb of the domain 3 anitform. Inset cross-polarized microscope image illustrates the deformation of the quartz ribbons during static recrystallization. Thin-section ~ 45mm in length.

12B-40
Luecogranite sill Xs(X(A)qf) in thin section.

Figure 28:   Full section scan of the garnet-rich leucocratic migmatite sample MT11-01 from ~ 5km south of the map area. Inset cross-polarized microscope images illustrate garnet replaced by biotite and plagioclase. Thin-section ~ 45mm in length.

MT11-01
Garnetiferous migmatite in thin section.

Table 1A:

Complete monazite analyses dataset (1A-1D)

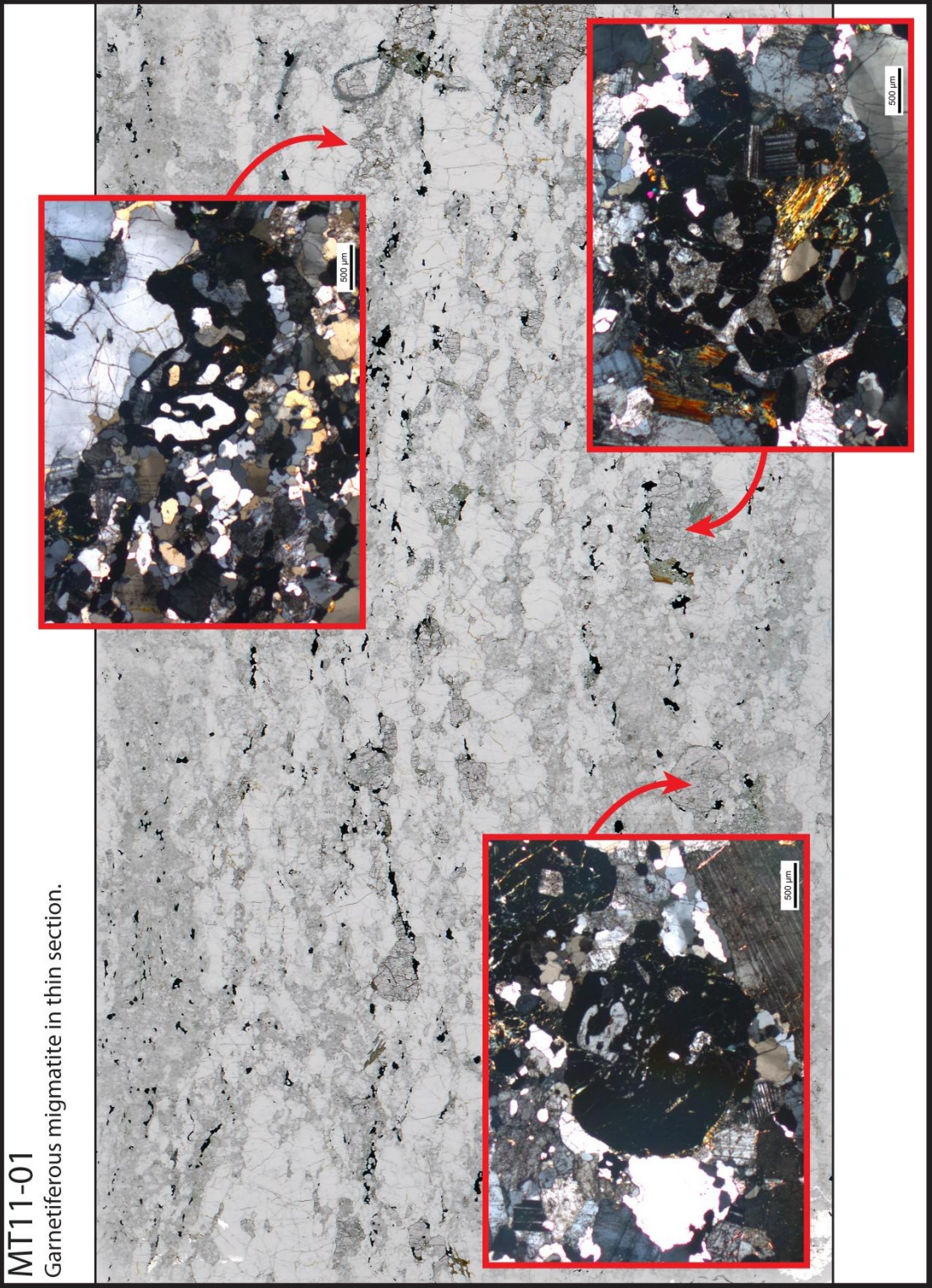| SAMPLE	Description	LINE	U WT%	Th WT%	Pb WT%	U PPM	Th PPM	Pb PPM	Date[My]	1σ	2σ
M1 Core A	Un 7 GD-12b-46b m1 hiY core right	404	0.174988	5.11576	0.733464	1749.88	51157.6	7334.64	2652.20		
M1 Core A	Un 7 GD-12b-46b m1 hiY core right	405	0.223276	3.81668	0.590407	2232.76	38166.8	5904.07	2634.00		
M1 Core A	Un 7 GD-12b-46b m1 hiY core right	406	0.215728	3.94953	0.627968	2157.28	39495.3	6279.68	2728.60		
M1 Core A	Un 7 GD-12b-46b m1 hiY core right	407	0.227298	3.85916	0.628976	2272.98	38591.6	6289.76	2753.30		
M1 Core A	Un 7 GD-12b-46b m1 hiY core right	408	0.217221	4.29977	0.649986	2172.21	42997.7	6499.86	2642.50		
M1 Core A	Un 7 GD-12b-46b m1 hiY core right	409	0.279098	5.90227	0.9017	2790.98	59022.7	9017	2693.40		
M1 Core A	Average Date								2684.00	49.22	98.44
M1 Core B	Un 6 GD-12b-46b m1 central core	398	0.148443	6.188	0.843638	1484.43	61880	8436.38	2621.40		
M1 Core B	Un 6 GD-12b-46b m1 central core	399	0.137243	6.10143	0.852031	1372.43	61014.3	8520.31	2692.90		
M1 Core B	Un 6 GD-12b-46b m1 central core	400	0.114459	5.30677	0.712433	1144.59	53067.7	7124.33	2606.30		
M1 Core B	Un 6 GD-12b-46b m1 central core	401	0.128849	5.69569	0.76707	1288.49	56956.9	7670.7	2604.40		
M1 Core B	Un 6 GD-12b-46b m1 central core	402	0.142688	6.04301	0.827333	1426.88	60430.1	8273.33	2634.80		
M1 Core B	Un 6 GD-12b-46b m1 central core	403	0.142103	6.11426	0.840972	1421.03	61142.6	8409.72	2649.30		
M1 Core B	Average Date								2634.85	33.17	66.34
M1 Rim	Un 23 GD-12b-46b m1 rim lower right	505	0.568091	14.0978	1.16904	5680.91	140978	11690.4	1570.40		
M1 Rim	Un 23 GD-12b-46b m1 rim lower right	507	0.266784	11.02	0.886666	2667.84	110200	8866.66	1603.00		
M1 Rim	Un 23 GD-12b-46b m1 rim lower right	508	0.472525	14.5082	1.15594	4725.25	145082	11559.4	1547.70		
M1 Rim	Un 23 GD-12b-46b m1 rim lower right	509	0.491656	15.112	1.20968	4916.56	151120	12096.8	1554.70		
M1 Rim	Un 23 GD-12b-46b m1 rim lower right	510	0.438728	13.8388	1.09568	4387.28	138388	10956.8	1542.50		
M1 Rim	Average Date								1563.66	24.37	48.74
M4 Core A	Un 18 GD-12b-46b m4 low Th inner core	470	0.329341	6.36421	0.916288	3293.41	63642.1	9162.88	2521.70		
M4 Core A	Un 18 GD-12b-46b m4 low Th inner core	471	0.331246	6.32063	0.972987	3312.46	63206.3	9729.87	2670.00		
M4 Core A	Un 18 GD-12b-46b m4 low Th inner core	472	0.327869	7.05935	1.03069	3278.69	70593.5	10306.9	2594.30		
M4 Core A	Un 18 GD-12b-46b m4 low Th inner core	473	0.315693	7.04501	0.987911	3156.93	70450.1	9879.11	2515.00		
M4 Core A	Un 18 GD-12b-46b m4 low Th inner core	474	0.327321	6.84569	1.01843	3273.21	68456.9	10184.3	2626.70		
M4 Core A	Un 18 GD-12b-46b m4 low Th inner core	475	0.330512	6.59564	0.938241	3305.12	65956.5	9382.41	2507.00		
M4 Core A	Un 18 GD-12b-46b m4 low Th inner core	476	0.337355	7.04984	0.974601	3373.55	70498.4	9746.01	2460.40		
M4 Core A	Average Date								2556.44	75.12	150.24
M4 Rim A	Un 20 GD-12b-46b m4 high Th rim upper	484	0.406974	15.9401	1.93612	4069.74	159401	19361.2	2346.70		
M4 Rim A	Un 20 GD-12b-46b m4 high Th rim upper	485	0.468204	16.3927	2.09953	4682.04	163927	20995.3	2439.20		
M4 Rim A	Un 20 GD-12b-46b m4 high Th rim upper	486	0.433001	16.5022	2.03502	4330.01	165022	20350.2	2374.10		
M4 Rim A	Un 20 GD-12b-46b m4 high Th rim upper	487	0.449163	16.7619	2.01709	4491.63	167619	20170.9	2317.10		
M4 Rim A	Un 20 GD-12b-46b m4 high Th rim upper	488	0.448106	16.8675	1.9814	4481.06	168675	19814	2268.00		
M4 Rim A	Un 20 GD-12b-46b m4 high Th rim upper	489	0.470697	17.417	2.07816	4706.97	174170	20781.6	2297.40		
M4 Rim A	Average Date								2340.42	60.94	121.89
M4 Rim B	Un 19 GD-12b-46b m4 higher Th right side	477	0.265863	9.29198	1.1419	2658.63	92919.8	11419	2348.30		
M4 Rim B	Un 19 GD-12b-46b m4 higher Th right side	478	0.293781	9.9753	1.15281	2937.81	99753	11528.1	2213.30		
M4 Rim B	Un 19 GD-12b-46b m4 higher Th right side	479	0.271007	9.85607	1.14977	2710.07	98560.7	11497.7	2246.60		
M4 Rim B	Un 19 GD-12b-46b m4 higher Th right side	480	0.265608	9.44967	1.00448	2656.08	94496.7	10044.8	2057.20		
M4 Rim B	Un 19 GD-12b-46b m4 higher Th right side	481	0.224222	8.68036	0.974872	2242.22	86803.6	9748.72	2180.80		
M4 Rim B	Un 19 GD-12b-46b m4 higher Th right side	482	0.211714	8.59965	0.935887	2117.14	85996.5	9358.87	2126.40		
M4 Rim B	Un 19 GD-12b-46b m4 higher Th right side	483	0.269042	9.51742	0.990831	2690.42	95174.2	9908.31	2016.70		
M4 Rim B	Average Date								2169.90	113.85	227.71
M5 Core A	Un 16 GD-12b-46b m5 hiY inner core upper	456	0.341384	7.27552	1.01729	3413.84	72755.2	10172.9	2492.60		
M5 Core A	Un 16 GD-12b-46b m5 hiY inner core upper	457	0.431226	7.55838	1.0869	4312.26	75583.8	10869	2480.10		

Table 1B:

Complete monazite analyses dataset (1A-1D)

SAMPLE	Description	LINE	U WT%	Th WT%	Pb WT%	U PPM	Th PPM	Pb PPM	Date[My]	1σ	2σ
M5 Core A	Un 16 GD-12b-46b m5 hiY inner core upper	458	0.30791	6.97228	0.931721	3079.1	69722.8	9317.21	2413.30		
M5 Core A	Un 16 GD-12b-46b m5 hiY inner core upper	459	0.375205	6.49587	0.972568	3752.05	64958.7	9725.68	2565.00		
M5 Core A	Un 16 GD-12b-46b m5 hiY inner core upper	460	0.423216	7.96037	1.04925	4232.16	79603.7	10492.5	2320.60		
M5 Core A	Un 16 GD-12b-46b m5 hiY inner core upper	461	0.329999	7.33115	0.972155	3299.99	73311.5	9721.55	2390.40		
M5 Core A	Average Date								2443.67	86.43	172.85
M5 Core B	Un 17 GD-12b-46b m5 hiTh mantle left	462	0.741924	17.6674	2.26163	7419.24	176674	22616.3	2336.80		
M5 Core B	Un 17 GD-12b-46b m5 hiTh mantle left	463	0.716742	17.463	1.97565	7167.42	174630	19756.5	2093.60		
M5 Core B	Un 17 GD-12b-46b m5 hiTh mantle left	464	0.685096	16.9811	2.12639	6850.96	169811	21263.9	2302.10		
M5 Core B	Un 17 GD-12b-46b m5 hiTh mantle left	465	0.740224	17.4109	2.16841	7402.24	174109	21684.1	2275.60		
M5 Core B	Un 17 GD-12b-46b m5 hiTh mantle left	466	0.737805	17.0331	2.19086	7378.05	170331	21908.6	2337.50		
M5 Core B	Un 17 GD-12b-46b m5 hiTh mantle left	467	0.719688	16.5248	2.09011	7196.88	165248	20901.1	2300.50		
M5 Core B	Un 17 GD-12b-46b m5 hiTh mantle left	468	0.719063	15.9146	1.95244	7190.63	159146	19524.4	2226.60		
M5 Core B	Un 17 GD-12b-46b m5 hiTh mantle left	469	0.695591	15.7561	2.05623	6955.91	157561	20562.3	2362.40		
M5 Core B	Average Date								2279.39	86.06	172.12
M5 RimA	Un 15 GD-12b-46b m5 low Y and Ca rim top	449	0.577961	11.4579	0.884904	5779.61	114579	8849.05	1425.80		
M5 RimA	Un 15 GD-12b-46b m5 low Y and Ca rim top	450	0.562987	11.0374	0.899564	5629.87	110374	8995.64	1497.90		
M5 RimA	Un 15 GD-12b-46b m5 low Y and Ca rim top	451	0.549358	11.152	0.913281	5493.58	111520	9132.81	1512.10		
M5 RimA	Un 15 GD-12b-46b m5 low Y and Ca rim top	452	0.54033	10.5961	0.885197	5403.3	105961	8851.97	1533.10		
M5 RimA	Un 15 GD-12b-46b m5 low Y and Ca rim top	453	0.545398	10.5422	0.884427	5453.98	105422	8844.27	1536.00		
M5 RimA	Un 15 GD-12b-46b m5 low Y and Ca rim top	454	0.549501	10.8659	0.904777	5495.01	108659	9047.77	1530.20		
M5 RimA	Un 15 GD-12b-46b m5 low Y and Ca rim top	455	0.535226	10.9306	0.902958	5352.26	109306	9029.58	1525.80		
M5 RimA	Average Date								1508.70	38.94	77.87
M5 RimB	Un 14 GD-12b-46b m5 low Y and Ca rim bottom	443	0.536233	10.5739	0.83214	5362.33	105739	8321.4	1450.30		
M5 RimB	Un 14 GD-12b-46b m5 low Y and Ca rim bottom	444	0.584412	11.2382	0.898807	5844.12	112382	8988.07	1467.20		
M5 RimB	Un 14 GD-12b-46b m5 low Y and Ca rim bottom	445	0.578254	11.2404	0.902404	5782.54	112404	9024.04	1474.80		
M5 RimB	Un 14 GD-12b-46b m5 low Y and Ca rim bottom	446	0.560151	10.7984	0.896026	5601.51	107984	8960.26	1519.70		
M5 RimB	Un 14 GD-12b-46b m5 low Y and Ca rim bottom	447	0.533501	10.6274	0.837364	5335.01	106274	8373.64	1454.10		
M5 RimB	Un 14 GD-12b-46b m5 low Y and Ca rim bottom	448	0.545569	10.6759	0.90004	5455.69	106759	9000.4	1545.80		
M5 RimB	Average Date								1485.32	38.68	77.36
M6 Core	Un 13 GD-12b-46b m6 center grain core right	437	1.04002	15.2899	1.36908	10400.2	152899	13690.8	1560.80		
M6 Core	Un 13 GD-12b-46b m6 center grain core right	438	1.10867	15.4665	1.41047	11086.7	154665	14104.7	1572.20		
M6 Core	Un 13 GD-12b-46b m6 center grain core right	439	0.954412	16.016	1.30677	9544.12	160160	13067.7	1463.70		
M6 Core	Un 13 GD-12b-46b m6 center grain core right	440	1.13091	15.5044	1.3533	11309.1	155044	13533	1504.10		
M6 Core	Un 13 GD-12b-46b m6 center grain core right	441	1.14466	16.0481	1.47124	11446.6	160481	14712.4	1581.40		
M6 Core	Un 13 GD-12b-46b m6 center grain core right	442	1.02549	16.347	1.4086	10254.9	163470	14086	1527.50		
M6 Core	Average Date								1534.95	45.38	90.76
M6 Rim	Un 21 GD-12b-46b m6 center grain low Y rims	490	0.687342	12.2968	0.965473	6873.42	122968	9654.73	1426.10		
M6 Rim	Un 21 GD-12b-46b m6 center grain low Y rims	491	0.700818	12.3752	1.02239	7008.18	123752	10223.9	1493.30		
M6 Rim	Un 21 GD-12b-46b m6 center grain low Y rims	492	0.574137	11.9956	0.952385	5741.37	119956	9523.85	1474.40		
M6 Rim	Un 21 GD-12b-46b m6 center grain low Y rims	493	0.818582	14.1789	1.17315	8185.82	141789	11731.5	1490.70		
M6 Rim	Un 21 GD-12b-46b m6 center grain low Y rims	494	0.800176	14.29	1.17586	8001.76	142900	11758.6	1490.20		
M6 Rim	Un 21 GD-12b-46b m6 center grain low Y rims	495	0.726368	12.9922	1.08054	7263.68	129922	10805.4	1505.60		
M6 Rim	Un 21 GD-12b-46b m6 center grain low Y rims	496	0.694106	13.8445	1.1026	6941.06	138445	11026	1469.20		
M6 Rim	Average Date								1478.50	26.10	52.21
M7 Core A	Un 4 GD-12b-46b m7 low Th inner core	384	0.722926	14.7518	2.14192	7229.26	147518	21419.2	2561.50		

Table 1C:

Complete monazite analyses dataset (1A-1D)

SAMPLE	Description	LINE	U WT%	Th WT%	Pb WT%	U PPM	Th PPM	Pb PPM	Date[My]	1σ	2σ
M7 Core A	Un 4 GD-12b-46b m7 low Th inner core	385	0.725888	14.7369	2.17236	7258.88	147369	21723.6	2594.30		
M7 Core A	Un 4 GD-12b-46b m7 low Th inner core	386	0.716413	14.6936	2.15594	7164.13	146936	21559.4	2587.40		
M7 Core A	Un 4 GD-12b-46b m7 low Th inner core	387	0.72173	14.7227	2.13731	7217.3	147227	21373.1	2561.00		
M7 Core A	Un 4 GD-12b-46b m7 low Th inner core	388	0.715003	14.6103	2.14042	7150.03	146103	21404.2	2582.40		
M7 Core A	Un 4 GD-12b-46b m7 low Th inner core	389	0.69483	14.5044	2.11169	6948.3	145044	21116.9	2576.20		
M7 Core A	Un 4 GD-12b-46b m7 low Th inner core	390	0.693011	14.5351	2.10421	6930.11	145351	21042.1	2565.00		
M7 Core A	Un 4 GD-12b-46b m7 low Th inner core	391	0.694812	14.637	2.09284	6948.12	146370	20928.4	2538.50		
M7 Core A	Average Date								2570.79	17.93	35.86
M7 Core B	Un 5 GD-12b-46b m7 mid Th core upper	392	0.819195	16.9159	2.4377	8191.95	169159	24377	2549.00		
M7 Core B	Un 5 GD-12b-46b m7 mid Th core upper	393	0.821938	16.8745	2.43329	8219.38	168745	24332.9	2548.10		
M7 Core B	Un 5 GD-12b-46b m7 mid Th core upper	394	0.828378	16.9279	2.47158	8283.78	169279	24715.8	2574.70		
M7 Core B	Un 5 GD-12b-46b m7 mid Th core upper	395	0.825252	17.0246	2.43479	8252.52	170246	24347.9	2531.30		
M7 Core B	Un 5 GD-12b-46b m7 mid Th core upper	396	0.824339	17.0009	2.47727	8243.39	170009	24772.7	2573.60		
M7 Core B	Un 5 GD-12b-46b m7 mid Th core upper	397	0.815921	16.9617	2.44418	8159.21	169617	24441.8	2551.20		
M7 Core B	Average Date								2554.65	16.69	33.38
M7 Rim A	Un 3 GD-12b-46b m7 rim upper right	376	0.638045	14.4602	2.08532	6380.45	144602	20853.2	2584.10		
M7 Rim A	Un 3 GD-12b-46b m7 rim upper right	377	0.642447	14.5128	2.09078	6424.47	145128	20907.8	2580.60		
M7 Rim A	Un 3 GD-12b-46b m7 rim upper right	379	0.644564	14.5134	2.07666	6445.64	145134	20766.6	2563.80		
M7 Rim A	Un 3 GD-12b-46b m7 rim upper right	380	0.648018	14.5847	2.03199	6480.18	145847	20319.9	2503.40		
M7 Rim A	Un 3 GD-12b-46b m7 rim upper right	381	0.62892	14.4389	2.09055	6289.2	144389	20905.5	2597.90		
M7 Rim A	Un 3 GD-12b-46b m7 rim upper right	382	0.659194	14.7508	2.12788	6591.94	147508	21278.8	2580.30		
M7 Rim A	Un 3 GD-12b-46b m7 rim upper right	383	0.667579	14.6885	2.10886	6675.79	146885	21088.6	2563.40		
M7 Rim A	Average Date								2567.64	30.75	61.51
M7 Rim B	Un 10 GD-12b-46b m7 hi Y outer rim	423	0.359772	9.25039	1.03824	3597.72	92503.9	10382.4	2091.90		
M7 Rim B	Un 10 GD-12b-46b m7 hi Y outer rim	424	0.353369	9.57096	1.07618	3533.69	95709.6	10761.8	2108.10		
M7 Rim B	Un 10 GD-12b-46b m7 hi Y outer rim	426	0.373701	10.4499	1.17636	3737.01	104499	11763.6	2118.00		
M7 Rim B	Un 10 GD-12b-46b m7 hi Y outer rim	427	0.363542	10.6916	1.15472	3635.42	106916	11547.2	2049.60		
M7 Rim B	Average Date								2091.90	30.18	60.36
M7 Rim C	Un 11 GD-12b-46b m7 hi Ca outer rim lower left	428	0.701677	10.2002	0.966377	7016.77	102002	9663.77	1641.70		
M7 Rim C	Un 11 GD-12b-46b m7 hi Ca outer rim lower left	429	0.704272	10.521	1.01053	7042.72	105210	10105.3	1671.00		
M7 Rim C	Un 11 GD-12b-46b m7 hi Ca outer rim lower left	430	0.599846	12.4966	1.04952	5998.46	124966	10495.2	1554.00		
M7 Rim C	Un 11 GD-12b-46b m7 hi Ca outer rim lower left	431	0.720408	10.5942	1.01458	7204.08	105942	10145.8	1661.70		
M7 Rim C	Un 11 GD-12b-46b m7 hi Ca outer rim lower left	432	0.700633	10.4962	0.970496	7006.33	104962	9704.96	1613.70		
M7 Rim C	Un 11 GD-12b-46b m7 hi Ca outer rim lower left	433	0.721074	10.5362	1.01238	7210.74	105362	10123.8	1665.00		
M7 Rim C	Average Date								1634.52	44.65	89.30
Standard	Un 2 Moacyr 4-01-2013 5pm	370	0.084052	6.19964	0.14374	840.523	61996.4	1437.4	494.50		
Standard	Un 2 Moacyr 4-01-2013 5pm	371	0.079266	6.15425	0.144339	792.664	61542.5	1443.39	501.10		
Standard	Un 2 Moacyr 4-01-2013 5pm	372	0.078661	6.15653	0.145956	786.609	61565.3	1459.56	506.60		
Standard	Un 2 Moacyr 4-01-2013 5pm	373	0.078144	6.16246	0.143343	781.444	61624.6	1433.43	497.40		
Standard	Un 2 Moacyr 4-01-2013 5pm	374	0.082291	6.16033	0.14675	822.914	61603.3	1467.5	508.10		
Standard	Un 2 Moacyr 4-01-2013 5pm	375	0.082102	6.14408	0.142805	821.021	61440.8	1428.05	496.00		
Standard	Average Date								500.62	5.68	11.35
Standard	Un 8 Moacyr 4-01-2013 post	410	0.082284	6.11546	0.146421	822.839	61154.6	1464.21	510.50		
Standard	Un 8 Moacyr 4-01-2013 post	411	0.083501	6.10979	0.147158	835.014	61097.9	1471.58	513.20		
Standard	Un 8 Moacyr 4-01-2013 post	412	0.085881	6.15075	0.145196	858.807	61507.5	1451.96	502.60		

51

Table 1D:

Complete monazite analyses dataset (1A-1D)

SAMPLE	Description	LINE	U WT%	Th WT%	Pb WT%	U PPM	Th PPM	Pb PPM	Date[My]	1σ	2σ
Standard	Un 8 Moacyr 4-01-2013 post	413	0.084765	6.10132	0.146423	847.646	61013.2	1464.23	511.00		
Standard	Un 8 Moacyr 4-01-2013 post	414	0.087026	6.09812	0.1451	870.256	60981.2	1451	506.10		
Standard	Un 8 Moacyr 4-01-2013 post	415	0.086501	6.14271	0.146216	865.012	61427.1	1462.16	506.60		
Standard	Average Date								508.33	3.91	7.82
Standard	Un 9 Moacyr 4-02-2013 9am	416	0.076665	6.18217	0.143616	766.65	61821.7	1436.16	497.20		
Standard	Un 9 Moacyr 4-02-2013 9am	417	0.081047	6.11918	0.145102	810.468	61191.8	1451.02	506.00		
Standard	Un 9 Moacyr 4-02-2013 9am	418	0.080796	6.09201	0.145962	807.963	60920.1	1459.62	511.20		
Standard	Un 9 Moacyr 4-02-2013 9am	419	0.079353	6.16321	0.145312	793.525	61632.1	1453.12	503.70		
Standard	Un 9 Moacyr 4-02-2013 9am	420	0.085071	6.13614	0.146319	850.714	61361.4	1463.19	507.80		
Standard	Un 9 Moacyr 4-02-2013 9am	421	0.079548	6.11608	0.144925	795.477	61160.8	1449.25	506.00		
Standard	Average Date								506.94	4.24	8.48
Standard	Un 22 Moacyr 4-02-2013 post	497	0.080842	6.15282	0.148477	808.416	61528.2	1484.77	515.00		
Standard	Un 22 Moacyr 4-02-2013 post	498	0.082704	6.12504	0.147066	827.037	61250.4	1470.66	512.00		
Standard	Un 22 Moacyr 4-02-2013 post	499	0.077507	6.15226	0.146187	775.072	61522.6	1461.87	508.00		
Standard	Un 22 Moacyr 4-02-2013 post	500	0.078585	6.1794	0.146727	785.854	61794	1467.27	507.50		
Standard	Un 22 Moacyr 4-02-2013 post	501	0.081236	6.15419	0.145821	812.361	61541.9	1458.21	505.70		
Standard	Un 22 Moacyr 4-02-2013 post	502	0.080525	6.17283	0.147835	805.246	61728.3	1478.35	511.30		
Standard	Average Date								509.92	3.45	6.89
Standard	Un 25 Moacyr 4-03-2013 3pm	514	0.088342	6.17548	0.146314	883.415	61754.8	1463.14	504.00		
Standard	Un 25 Moacyr 4-03-2013 3pm	515	0.083037	6.14829	0.146674	830.375	61482.9	1466.74	508.60		
Standard	Un 25 Moacyr 4-03-2013 3pm	516	0.085633	6.1752	0.145969	856.332	61752	1459.69	503.50		
Standard	Un 25 Moacyr 4-03-2013 3pm	517	0.080566	6.14105	0.146744	805.658	61410.5	1467.44	510.00		
Standard	Un 25 Moacyr 4-03-2013 3pm	518	0.085624	6.17324	0.148939	856.243	61732.4	1489.39	513.70		
Standard	Un 25 Moacyr 4-03-2013 3pm	519	0.086319	6.17166	0.148155	863.19	61716.6	1481.55	511.00		
Standard	Average Date								508.47	4.02	8.04

52

Figure 29:

        Thorium Mα X-ray map of monazite grain M5 from thin section 12B-46B. Three distinct domains are apparent by variations in thorium concentration. Average dates are given in millions of year ago with errors of ±2σ standard deviation. Image is 300 x 300 pixels in dimension, each pixel is 0.596 μm in width.
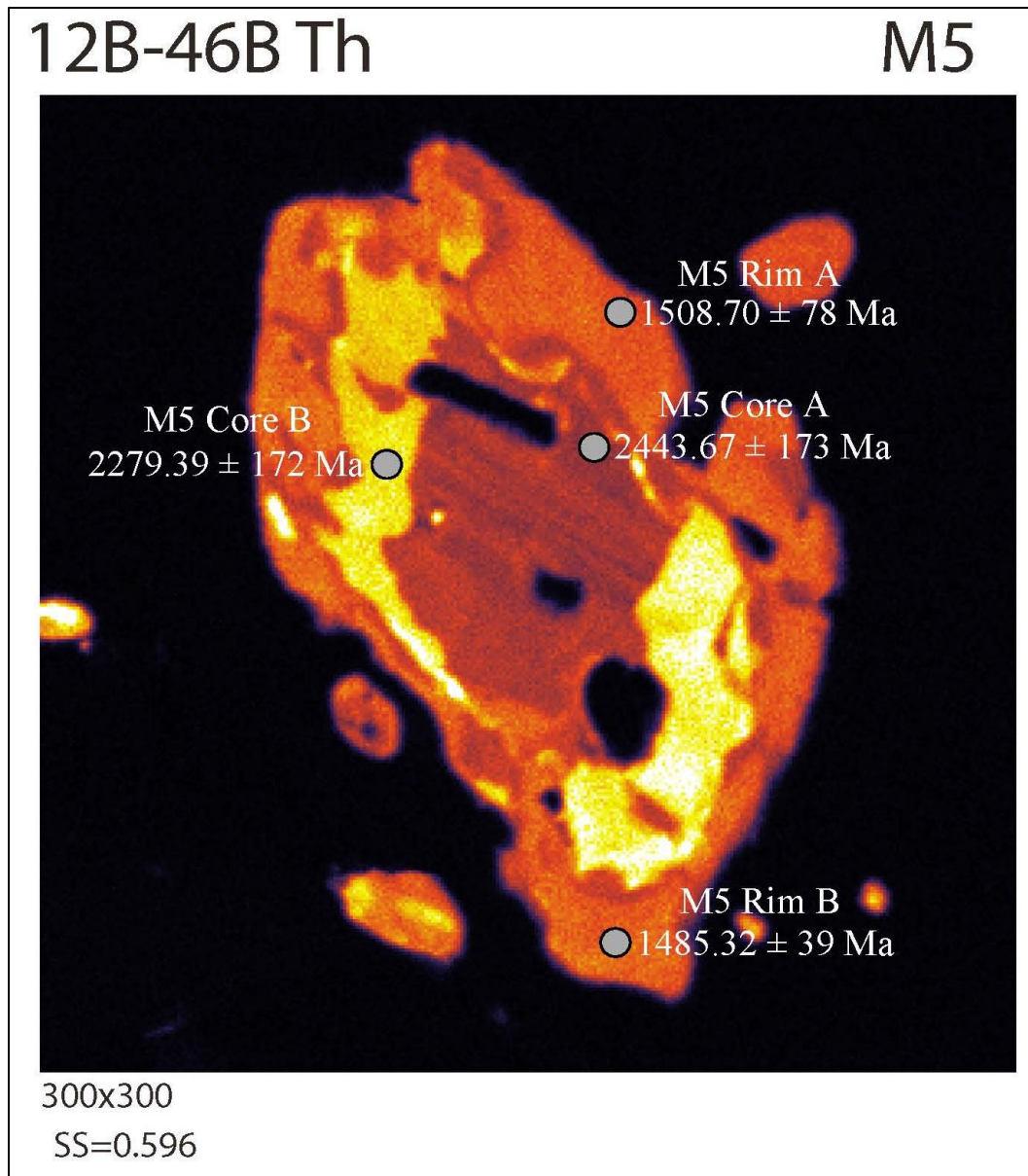
Figure 30:

Calcium Kα X-ray map of monazite grain M7 from thin section 12B-46B. At least three distinct domains are apparent by variations in calcium concentration and average date. Average dates are given in millions of year ago with errors of ±2σ standard deviation. Image is 500 x 500 pixels in dimension, each pixel is 0.572 μm in width.

Figure 31:
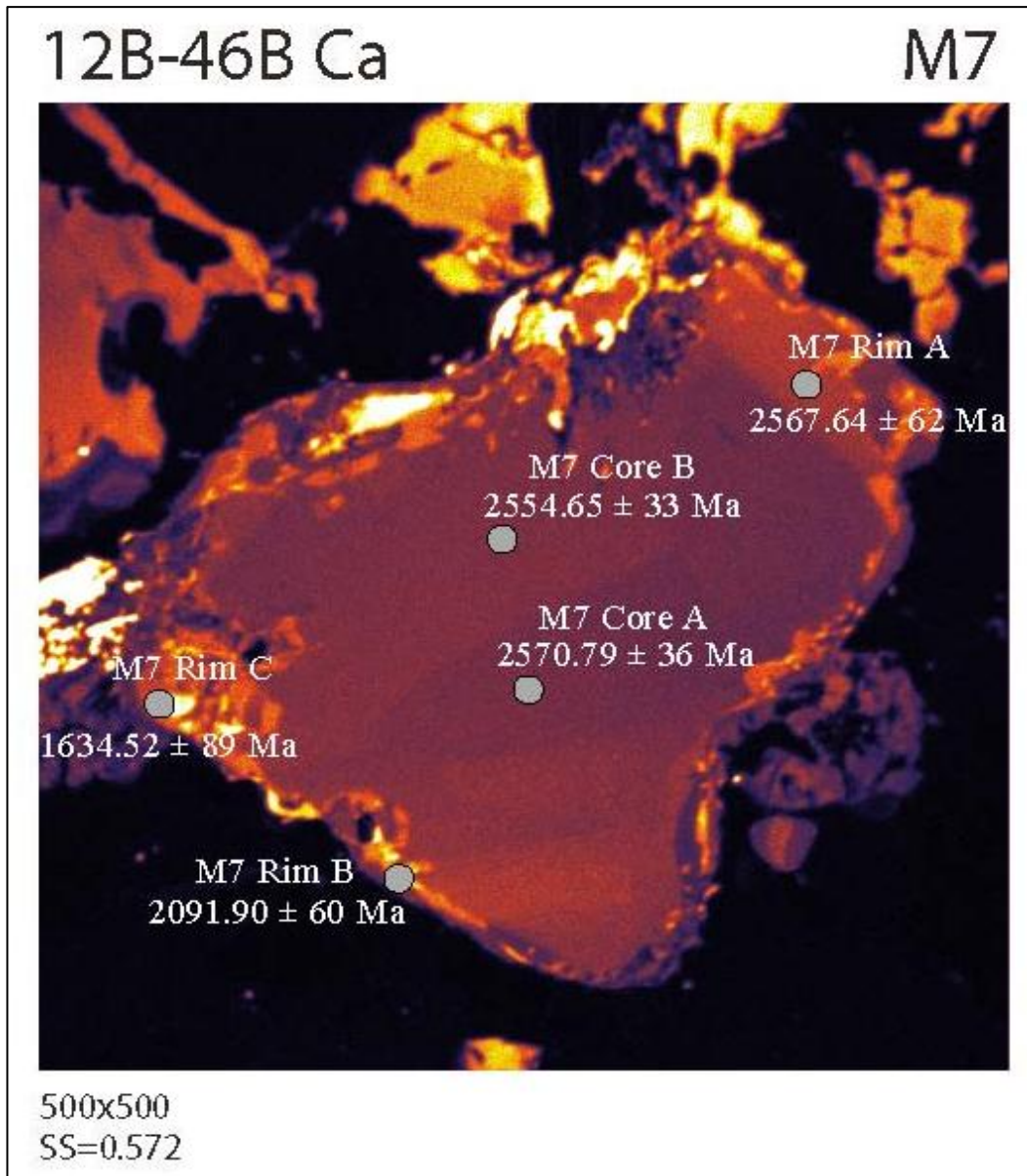
This figure is our preferred model for the collision of the GFTZ and the development of the Highland Mountains gneiss dome. The average stretching lineation as measured within the Steels Pass shear zone (22°→261°) conforms with the direction of extension resulting from a NW-SE oblique collision along the GFTZ (O'Neill et al., 1988; Mueller et al., 2005).
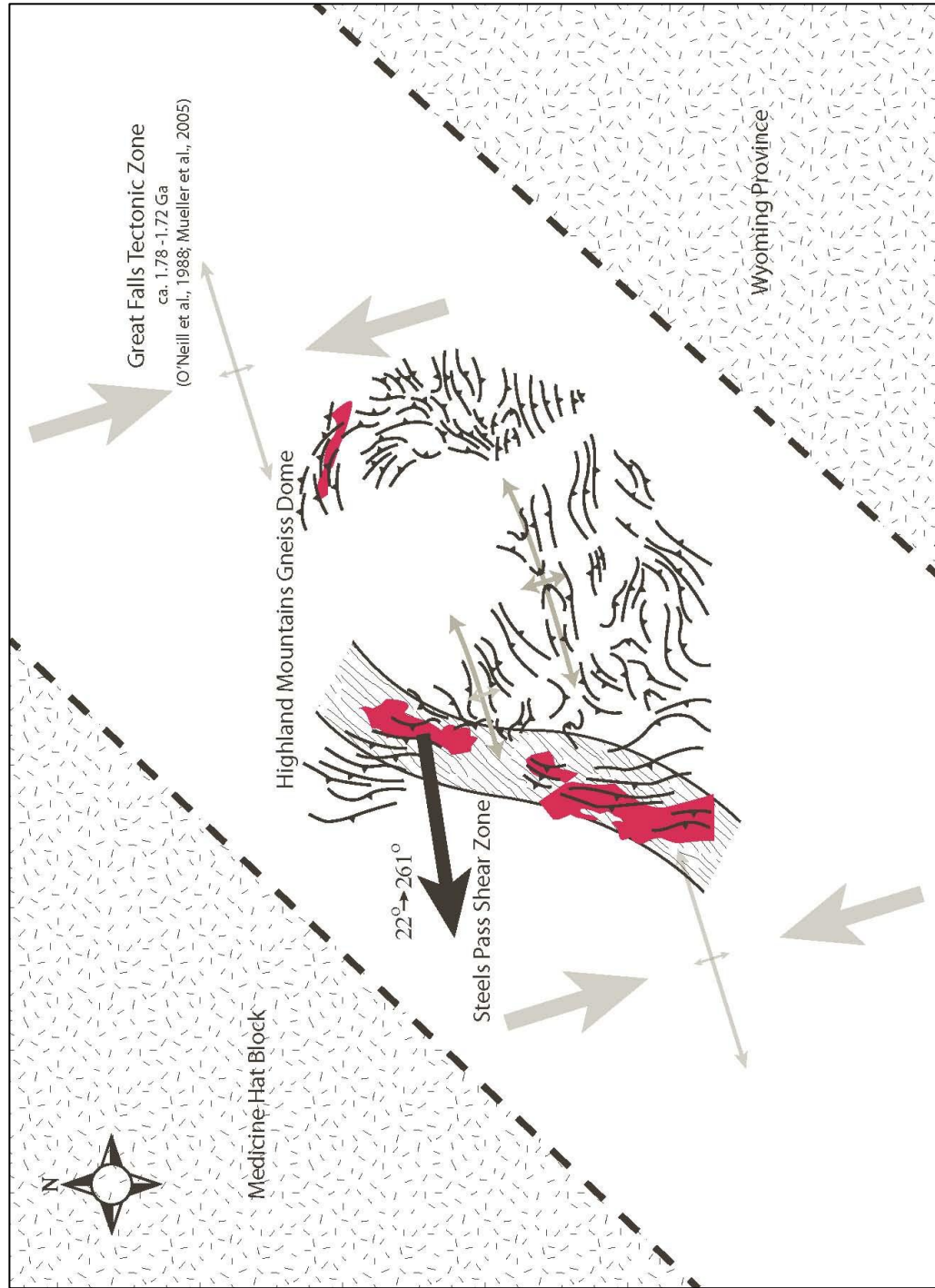
Figure 32:
    Full section scan of thin section 12B-45 sampled within the Steels Pass shear zone. Inset cross-polarized microscope images illustrate a large altered garnet with quartz ribbons conforming to its shape and the development of foam texture in the quartz and feldspar matrix grains as a result of static recrystallization. Thin-section ~ 45mm in length.

12B-45
Luecogranite sill Xs(X(A)qf) in thin section.
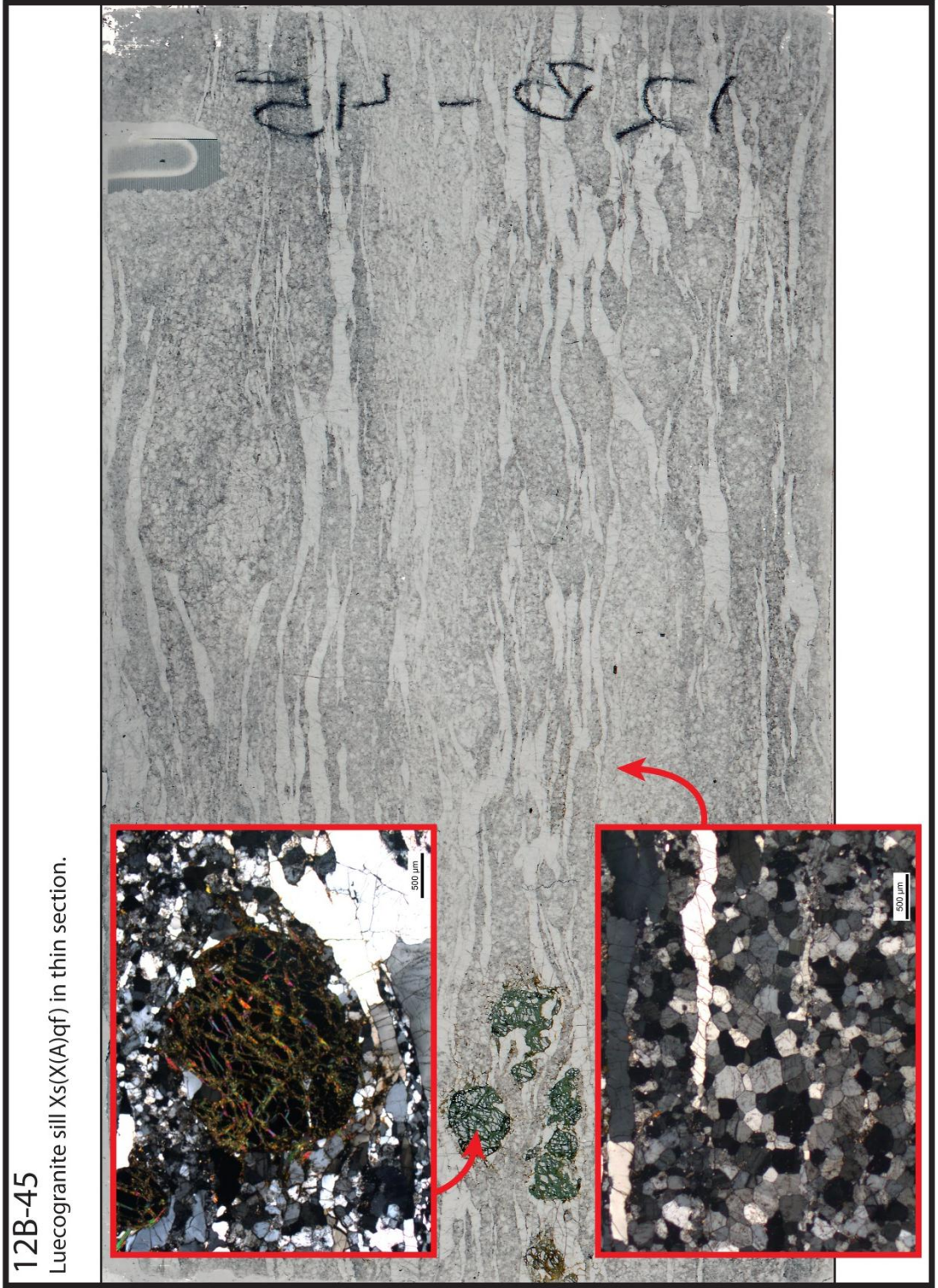
IX. References

Andronicos, C., Chardon, D., Hollister, L., Gehrels, G. and Woodsworth, G., 2003. Strain partitioning in an obliquely convergent orogen, plutonism, and synorogenic collapse: Coast Mountains Batholith, British Columbia, Canada. Tectonics 22(2): doi: 10.1029/2001TC001312. issn: 0278-7407.

Ault, K.A., Flowers, R.M., and Mahan, K.H., 2012-In Review. Quartz shielding of sub-20 μm zircons from radiation damage-enhanced Pb loss: an example from a granulite facies mafic dike, northwestern Wyoming craton. Earth and Planetary Science Letters.

Beaumont, C., Jamieson, R.A., Nguyen, M.H., and Medvedev, S., 2004. Crustal channel flows: 1. Numerical models with applications to the tectonics of the Himalayan-Tibetan orogen, J. Geophys. Res., 109, B06406, doi:10.1029/2003JB002809.

Beaumont, C., Jamieson, R. A., Nyugen, M.H. and Lee, B., 2001. Himalayan tectonics explained by extrusion of a low-viscosity channel coupled to focused surface denudation. *Nature*, 414, 738-742.

Bingen, B., and van Breemen, O., 1998. U-Pb monazite ages in amphibolite to granulite-facies orthogneiss reflect hydrous mineral breakdown reactions: Sveconorwegian Province of SW Norway. Contrib Miner Petrol 132:336–353.

Boerner, D., Craven, J., Kurtz, R., Ross, G., and Jones, F., 1998. The Great Falls tectonic zone: Suture or intracontinental shear zone?: Canadian Journal of Earth Sciences, v. 35, p. 175–183.

Chandler, F.W., 2000. The Belt-Purcell Basin as a low-latitude passive rift: Implications for the geological environment of Sullivan type deposits;Chapter 6, in Lydon, J.W., Höy, T., Slack, J.F., and Knapp, M., eds., The Geological Environment of the Sullivan Deposit, British Columbia, Geological Association of Canada, Mineral Deposits Division, Special Publication No. 1, p.82-112.

Chamberlain, K., 1998. Medicine Bow orogeny: Timing of deformation and model of crustal structure produced during continent-arc collision, ca. 1.78 Ga, southeastern Wyoming: Rocky Mountain Geologist, v. 33, p. 259–277.

Collins, W.J., 2002. Hot orogen, tectonic switching, and creation of continental crust. Geology, 30: 535-538.

Dahl, P., Holm, D., Gardner, E., Hubacher, F., and Foland, K., 1999. New constraints on the timing of Early Proterozoic tectonism in the Black Hills (South Dakota), with implications for docking of the Wyoming province with Laurentia: Geological Society of America Bulletin, v. 111, p. 1335–1349.

Davis, W.J., Berman, R., and Kyarsgaard, B., 1995. U-Pb geochronology and isotopic studies of crustal xenoliths from the Archean Medicine Hat block, northern Montana and souther Alberta: Paleoproterozoic reworking of Archean crust. *In* 1995 Alberta Basement Transects Workshop. *Edited by* G.M. Ross. Lithoprobe Secretariat, The University of British Columbia, Lithoprobe Report 47, pp.330-335.

Dumond, G., McLean, N., Williams, M.L., Jercinovic, M.J., and Bowring, S.A., 2008. High-resolution dating of granite petrogenesis and deformation in a lower crustal shear zone: Athabasca granulite terrane, western Canadian Shield. Chemical Geology 254, 175 – 196.

Erslev, E.A. and Sutter, J.F., 1990. Evidence for Proterozoic mylonitization in the northwestern Wyoming province: Geological Society of America Bulletin, v.102 p.1681-1694.

Evans, B., Renner, J., and Hirth, G., 2001. A few remarks on the kinetics of static grain growth in rocks. Int. Journal of Earth Sciences 90: 88-103.

Foster, D.A., Mueller, P.A., Mogk, D.W., Wooden, J.L., and Vogl, J.J., 2006. Proterozoic evolution of the western margin of the Wyoming craton: implications for the tectonic and magmatic evolution of the northern Rocky Mountains. Canadian Journal of Earth Sciences 43, 1601 – 1619.

Giletti, B.J., 1971. Discordant isotopic ages and excess argon in biotites: Earth and Planetary Science Letters, v. 10, p. 157–164.

Giletti, B., 1966. Isotopic ages from southwestern Montana: Journal of Geophysical Research, v. 71, p. 4029–4036.

Green, A., Hajnal, Z., and Weber, W., 1985. An evolutionary model for the western Churchill Province and western margin of the Superior Province in Canada and the north-central United States: Tectonophysics, v. 116, p. 281–322.

Hansen, E.C., and Harlov, D.E., 2007. Whole-rock, phosphate, and silicate compositional trends across an amphibolite- to granulite-facies transition, Tamil Nadu, India. J Petrol 48:1641–1680.

Harlan, S., Geissman, J., Snee, L., and Reynolds, R., 1996. Late Cretaceous remagnetization of Proterozoic mafic dikes, southern Highland Mountains, southwestern Montana: A paleomagnetic and 40Ar/39Ar study: Geological Society of America Bulletin, v. 108, p. 653–668.

Harlov, D.E., Wirth, R., and Hetherington, C.J., 2010. Fluid-mediated partial alteration in monazite: the role of coupled dissolution-reprecipitation in element redistribution and mass transfer. Springer-Verlag 2010. Contrib Mineral Petrol. DOI 10.1007/s00410-010-0599-7.

Harms, T.A., Brady, J.B., and Cheney, J.T., 2006. Exploring the Proterozoic Big Sky orogeny in

Southwest Montana. 19th annual Keck Symposium; http://keck.wooster.edu/publications.

Harms, T. A., Brady, J. B., Burger, H. R., and Cheney, J. T., 2004. Advances in the geology of the Tobacco Root Mountains, Montana, and their implications for the history of the northern Wyoming Province, , in J. B. Brady, H. R. Burger, J. T. Cheney and T. A. Harms (eds.), Precambrian Geology of the Tobacco Root Mountains, Montana, GSA Special Paper 377, pp. 227-246.

Hoffman, P., 1989. Speculations on Laurentia's first gigayear (2.0 to 1.0 Ga). Geology 17, 135-138.

Hoffman, P., 1988. United plates of America, the birth of a craton: Annual Reviews of Earth and Planetary Science, v. 16, p. 543–603.

Jercinovic, M.J., Williams, M.L., Lane, E.D., 2008. In situ trace element analysis in complex, multi-phase materials by EPMA. Chemical Geology 254, 197–215 (this issue). doi:10.1016/j.chemgeo.2008.05.016.

Jercinovic, M.J., Williams, M.L., 2005. Analytical perils (and progress) in electron microprobe trace element analysis applied to geochronology: background acquisition, interferences, and beam irradiation effects. American Mineralogist 90 (4), 526–546.

Karlstrom, K., and Houston, R., 1984. The Cheyenne Belt: Analysis of a Proterozoic suture in southern Wyoming: Precambrian Research, v. 25, p. 415–446.

Lemieux, S., Ross, G., and Cook, F., 2000. Crustal geometry and tectonic evolution of the Archean crystalline basement beneath the southern Alberta Plains, from new seismic reflection and potential-field studies: Canadian Journal of Earth Sciences, v. 37, p. 1473–1491.

Lydon, J.W., 2008. Synopsis of the Belt-Purcell Basin. Belt-Purcell Metallogeny. Mineral Resources Division, Geological Survey of Canada.

Martins L., Farias Vlach S.R., and de Assis Janasi, V., 2009. Reaction microtextures of monazite: correlation between chemical and age domains in the Nazare´ Paulista migmatite, SE Brazil. Chem. Geol 261:271–285.

Montel, J.M., Foret, S., Veschambre, M., Nicollet, C., and Provost, A., 1996. Electron microprobe dating of monazite. Chemical Geology 131 (1–4), 37–53.

Mueller, P.A., Burger, H.R., Wooden, J.L., Brady, J.B., Cheney, J.T., Harms, T.A., Heatherington, A.L., and Mogk, D.W., 2005. Paleoproterozoic metamorphism in the northern Wyoming Province: Implications for the assembly of Laurentia. Journal of Geology 113, 169 – 179.

Mueller, P.A., Heatherington, A.L., Kelly, D.M., Wooden, J.L., and Mogk, D.W., 2002. Paleoproterozoic crust within the Great Falls tectonic zone: Implications for the assembly of southern Laurentia. Geology; February 2002; v. 30; no. 2; p. 127–130.

Nelson, K., Baird, D., Walters, J., Hauck, M., Brown, L., Oliver, J., Ahern, J., Hajnal., Z., Jones, A., and Sloss, L., 1993. Trans-Hudson orogen and Williston basin beneath northeastern Montana and northern North Dakota: New COCORP deep profiling results: Geology, v. 21, p. 447–450.

O'Neill, J.M., 1998. The Great Falls tectonic zone, Montana-Idaho: an early Proterozoic collisional orogen beneath and south of the Belt Basin. *In* Belt Symposium III. *Edited by* R.B. Berg. Montana Bureau of Mines and Geology, Special Publication 112, 222 – 228.

O'Neill, J.M., Klepper, M.R., Smedes, H.W., Hanneman, D.L., Fraser, G.D., and Mehnert, H.H., 1996. Geologic Map and Cross Sections of the Central and Southern Highland Mountains, Southwestern Montana. U.S. Department of the Interior, U.S. Geological Survey, Miscellaneous Investigation Series, Map I-2525.

O'Neill, J.M., 1995, Early Proterozoic geology of the Highland Mountains, southwestern Montana, and field guide to the basement rocks that compose the Highland Mountain gneiss dome, in Mogk, D.W., ed., Field guide to geologic excursions in southwest Montana, Geological Society of America, Rocky Mountain Section: Northwest Geology, v. 24, p. 85–97.

O'Neill, J.M., Duncan, M.S., and Zartman, R.E., 1988. An Early Proterozoic gneiss dome in the Highland Mountains, southwestern Montana. *In* Precambrian and Mesozoic plate margins. *Edited by* S.E. Lewis and R.B. Berg Montana Bureau of Mines and Geology, Special Publication 96, 81 – 88.

O'Neill, J.M. and Lopez, D., 1985. Character and regional significance of Great Falls tectonic zone, East-Central Idaho and West-Central Montana. American Association of Petroleum Geologists Bulletin 69, 437 – 447.

Passchier, C.W., and Trouw, R.A.J., 2005. Micro-tectonics, 2nd edition. Springer, Berlin.

Pyle, J.M., Spear, F.S., Wark, D.A., Daniel, C.G., and Storm, L.C., 2005. Contributions to precision and accuracy of chemical ages of monazite. American Mineralogist 90: 547–577.

Rasmussen, B., and Muhling, J.R., 2007. Monazite begets monazite: evidence for dissolution of detrital monazite and reprecipitation of syntectonic monazite during low-grade regional metamorphism. Contrib Miner Petrol 154:675–689.

Simmat, R. and Raith, M.M., 2008. U-Th-Pb monazite geochronometry of the Eastern Ghats Belt, India: timing and spatial disposition of poly-metamorphism. Precamb Res 162:16–39.

Tullis, J. (2002). Deformation of Granitic Rocks: Experimental Studies and Natural Examples. Reviews in Mineralogy and Geochemistry. S. Karato and H.-R. Wenk. Washington, D.C., Mineralogical Society of America. 51: 51-96.

Williams, M.L., Jercinovic, M.J., Goncalves, P., and Mahan, K., 2006. Format and philosophy for collecting, compiling, and reporting microprobe monazite ages. Chemical Geology 225 (1/2), 1–15.

Williams, M.L., Jercinovic, M.J., and Hetherington, C.J., 2006a. Microprobe Monazite Geochronology: Understanding Geologic Processes by Integrating Composition and Chronology. Annu. Rev. Earth Planet. Sci. 2007. 35:137–75

Williams, M.L., and Jercinovic, M.J., 2002. Microprobe monazite geochronology: putting absolute time into microstructural analysis. Journal of Structural Geology 24 (6/7), 1013–1028.